

Fundamental Plane of BOSS galaxies: Correlations with galaxy properties, density field and impact on RSD measurements.

Sukhdeep Singh^{1*}, Byeonghee Yu¹, Uroš Seljak¹

¹ *Berkeley Center for Cosmological Physics, University of California, Berkeley, CA 94720, USA*

Accepted XXX. Received YYY; in original form ZZZ

ABSTRACT

Fundamental plane of elliptical galaxies can be used to predict the intrinsic size of galaxies and has a number of plausible application to study cosmology and galaxy physics. We present a detailed analysis of the fundamental plane of the SDSS-III BOSS LOWZ and CMASS galaxies. For the standard fundamental plane, we find a strong redshift evolution for the mean residual and show that it is primarily driven by the redshift evolution of the surface brightness of the galaxies. After correcting for the redshift evolution, the FP residuals are strongly correlated with the galaxy properties and some observational systematics. We show that the variations in the FP between the central and satellite galaxies, that have been observed in the literature, can primarily be explained by the correlation of the FP with the galaxy luminosity. We also measure the cross correlations of the FP residuals with the galaxy density field. The amplitude of the cross correlations depends on the galaxy properties and environment with brighter and redder galaxies showing stronger correlation. In general, galaxies in denser environments (higher galaxy bias) show stronger correlations. We also compare FP amplitude with the amplitudes of intrinsic alignments of galaxy shapes (IA), finding the two to be correlated. Finally, using the FP residuals we also study the impact of intrinsic alignments on the constraint of growth rate using redshift space distortions. We do not observe any significant trends in measurements of the growth rate f as function of the amplitude of FP-density correlations, resulting in null detection of the effects of IA on the RSD measurements.

Key words: cosmology; observations — large-scale structure of Universe — gravitational lensing; weak

1 INTRODUCTION

Fundamental Plane (FP) of galaxies, an empirical relation between the size, surface brightness and the velocity dispersion of early type galaxies, has been proposed as a cosmological probe to estimate distances to galaxies, galaxy velocities (Strauss & Willick 1995), weak gravitational lensing magnification (Bertin & Lombardi 2006), doppler magnification of galaxies (Bonvin et al. 2017), impact of intrinsic alignments on galaxy selection functions (Hirata 2009); in addition to its value as probe for galaxy physics.

For elliptical galaxies, a relation between the size, surface brightness and velocity dispersion can be derived from the virial theorem assuming constant mass to light ratio for the galaxies. Such relations have been observed for a long time (eg. Dressler et al. 1987; Djorgovski & Davis 1987;

Bernardi et al. 2003; Saulder et al. 2013, 2019), though the observed FP deviates significantly from the virial theorem predictions as the galaxies do not follow the simplified underlying assumptions. Furthermore FP has been observed to be a function of galaxy properties (eg. Scodeggio et al. 1998; Nigoche-Netro et al. 2009; Saulder et al. 2019) and their environment (de Carvalho & Djorgovski 1992; Joachimi et al. 2015; Saulder et al. 2019).

The cosmological prowess of the FP arises from its ability to provide an estimate of the true intrinsic size of the galaxies (with some scatter). The observed galaxy size is affected by several processes, including estimates of cosmological distances, peculiar motion of galaxies (since we estimate distance through redshift), relativistic effects including the doppler shift, gravitational lensing and the effects of projecting three dimensional shapes onto the plane of the sky. Once the intrinsic size of a galaxy is known, the difference between the observed and the true size of the galaxies (hereby size

* E-mail: sukhdeep1@berkeley.edu

residual or FP residual) can be used to study several of these effects. The size residuals can provide a (noisy) estimate of the peculiar velocity of individual galaxies which can be used to map the cosmological flows (Strauss & Willick 1995). Cross correlations of the size residuals with the foreground galaxies (or clusters) can be also be used to measure the galaxy-lensing cross correlations (Bertin & Lombardi 2006; Huff & Graves 2011). Bonvin et al. (2017) also suggested measuring the dipole of the galaxy-size residual cross correlations to estimate the doppler magnification of the galaxies. Hirata (2009) pointed out that due to the radial intrinsic alignment of galaxies and the projection effects, the size residuals are correlated with the local galaxy environment and if the selection function for a galaxy survey is sensitive to such residuals, it can introduce biases into measurements of redshift anisotropy of the galaxy auto correlations. Such an effect was tentatively detected by Martens et al. (2018) using the fundamental plane of SDSS-III BOSS galaxies.

However, as pointed out earlier, the FP depends on the galaxy properties and their environment (eg. de Carvalho & Djorgovski 1992; Scodreggio et al. 1998; Nigoche-Netro et al. 2009; Joachimi et al. 2015; Saulder et al. 2019). Joachimi et al. (2015) detected the cross correlations between the FP residuals and the galaxy density field implying that the FP residuals are influenced by the galaxy environment. They further detected the dependence of the FP residuals on the galaxy type, with the brightest galaxies in groups having larger sizes than predicted by the FP while the satellite galaxies have smaller sizes. Such dependence of the FP residuals on the galaxy environment complicates the cosmological applications of the FP and detailed studies are required to understand such dependencies and avoid possible contamination to the cosmological inferences.

In this work, we extend the FP analysis from Joachimi et al. (2015) to the BOSS LOWZ and CMASS sample galaxies. We estimate the fundamental plane for these samples as well as for sub-samples using splits based on color, luminosity and environment of the galaxies. We also study the cross correlations between FP residuals and galaxy density field and compare these cross correlations to those expected from the effects of intrinsic alignments as pointed out by Hirata (2009). Finally we also perform a detailed study of contamination to the galaxy clustering measurements from the radial alignments, similar to the analysis by Martens et al. (2018), in an attempt to confirm their results.

Throughout this work we will use flat Λ CDM model with the Planck 2015 (Planck Collaboration et al. 2015) cosmology with $h = 0.677$, $\Omega_m = 0.307$. Unless mentioned otherwise, distances are measured in unit of comoving h^{-1} Mpc. To compute the matter power spectrum, we use CLASS code (Lesgourgues 2011) with halofit (Takahashi et al. 2012) prescription for the non-linear matter power spectrum. For redshift-space galaxy power spectrum calculations, we employ the FFT-based algorithm implemented in `nbbodykit` (Hand et al. 2018), and use `pyRSD` (Hand et al. 2017b) to compute the theoretical predictions of the redshift-space power spectrum of galaxies and run a likelihood analysis to find the best-fit theory model parameters.

2 FORMALISM

In this section we describe our formalism used in the estimation of fundamental plane and the residuals over it (size or FP residuals); the estimators and models used to study the cross-correlation between FP residuals and the density field; the power spectra and modeling of the redshift space galaxy clustering.

2.1 Fundamental Plane

To estimate the fundamental plane of galaxies (FP), we closely follow the methodology from Saulder et al. (2013) and Joachimi et al. (2015). We define the FP as

$$\log R_0 = a \log \sigma_0 + b \log I_0 + c + \sum_{i=1}^{N_z} d_i z_{cor}^i, \quad (1)$$

where R_0 is the physical radius of the galaxy, I_0 is the surface brightness and σ_0 is the velocity dispersion. Following Joachimi et al. (2015), we also introduce polynomial terms dependent on the redshift of the galaxies. z_{cor} is the redshift of the galaxies in the CMB rest frame (correcting for the motion of the earth with rest to CMB rest frame) and is estimated as detailed in Saulder et al. (2013).

The physical size of the galaxy, R_0 , is measured as (in units of kpc/h)

$$r_{cor} = r_0 \sqrt{q_{b/a}} \quad (2)$$

$$R_0 = D_A(z_{cor}) \tan(r_{cor}) \times 1000 \quad (3)$$

where r_0 is the angular galaxy size and $q_{b/a}$ is the axis ratio which is used to measure the circularized galaxy size, r_{cor} (Bernardi et al. 2003; Saulder et al. 2013), with both r_0 and $q_{b/a}$ measured using the de Vaucouleurs profile. $D_A(z)$ is the angular diameter distance in units of Mpc/h.

The surface brightness, I_0 , is computed as

$$\log I_0 = -\frac{1}{2.5} \left[M_{ke} + 5 \log \left(\frac{D_L}{D_{L0}} \right) \right] - \log(2\pi R_0) + 4 \log(1+z_{cor}) \quad (4)$$

M_{ke} is the $k + e$ corrected absolute magnitude as defined in Singh et al. (2015), $\frac{D_L}{D_{L0}}$ is the correction to the luminosity distance due to redshift correction (D_L is estimated using z_{cor} while D_{L0} is estimated using measured redshift in observer frame). $4 \log(1+z_{cor})$ factor corrects for the cosmological dimming of the surface brightness (Tolman 1930).

We also correct the velocity dispersion, σ_0 , for the effects of the fiber size (different correction for BOSS and SDSS spectra) as (Saulder et al. 2013)

$$\sigma_0 = \sigma \left(\frac{r_{\text{fiber}}}{r_{cor}/8} \right)^{0.04} \quad (5)$$

where $r_{\text{fiber}} = 1''$ for BOSS and $r_{\text{fiber}} = 1.5''$ for SDSS spectrographs. We identify the spectrograph from the date the spectra for the given galaxy was obtained and then apply the relevant correction.

FP residual for a galaxy is defined in terms of the fractional difference between the measured size and the size predicted using FP,

$$\lambda_{N_z} = \ln \frac{R_0}{R_{FP,N_z}} = \log R_0 - a \log \sigma_0 - b \log I_0 - c - \sum_{i=1}^{N_z} d_i z_{cor}^i,$$

(6)

where N_z refers to the order of polynomial used for fitting the FP as defined in eq. (1). We find that the upto third order polynomials in z in eq. (1) are not necessarily sufficient to fully null the redshift evolution of the λ . To further reduce the effects of redshift evolution, we also fit the FP in redshift bins and will denote λ from such fits as λ^{z^b} . We typically use bins with width $\delta z = 0.02$ for such fits to obtain $\lambda_{N_z}^{z^b}$ for all galaxies and will subsequently carry out the following analysis in the same manner as λ (i.e. ignoring z binning).

Martens et al. (2018) ignored the velocity dispersion measurements in their FP analysis. To study the influence of velocity dispersion, we also define

$$\log R_0 = b^I \log I_0 + c^I + \sum_{i=1}^{N_z} d_i^I z^i \quad (7)$$

$$\lambda_{N_z}^I = \ln \frac{R_0}{R_{\text{FP}, N_z}^I} \quad (8)$$

where we used superscript I to denote that the FP is only dependent on surface brightness and not the velocity dispersion. We note that this FP definition is not strictly equivalent to the FP definition used by Martens et al. (2018) who defined the FP using magnitudes instead of surface brightness. We will present detailed comparisons with the Martens et al. (2018) results in appendix A.

2.2 Galaxy-Galaxy correlations

2.2.1 Estimator

To compute the galaxy-galaxy cross-correlation function between two different samples, we use the Landy-Szalay estimator (Landy & Szalay 1993; Singh et al. 2017)

$$\xi_{gg}(r_p, \Pi) = \frac{SD - DR_S - SR_D + R_S R_D}{R_S R_D}, \quad (9)$$

where r_p is the projected separation for a pair of galaxies, Π is the line of sight separation, D and S refers to the dataset (galaxies) being cross correlated ($D = S$ in case of auto correlations) and R_S and R_D refer to the set of random points corresponding to S and D samples. Product XY (eg. SD) refers to the binned weighted count of pairs across two samples with distances that are within the (r_p, Π) range of the given bin. The weight of a pair is the product of the galaxy weights that are described in section 3.

The projected correlation function is then obtained by integrating ξ_{gg} over the bins in Π

$$w_{gg}(r_p) = \sum_{-\Pi_{\max}}^{\Pi_{\max}} \Delta \Pi \xi_{gg}(r_p, \Pi). \quad (10)$$

Large values of Π_{\max} are required to reduce the impact of redshift space distortions (RSD) on measured correlation function, even though measurement noise increases with larger Π_{\max} (Singh et al. 2017). To reduce the impact of redshift space distortions on the projected correlations, we use $\Pi_{\max} = 100h^{-1}\text{Mpc}$, with 20 bins of size $\Delta \Pi = 10h^{-1}\text{Mpc}$.

Separately, to analyze the line of sight anisotropy, we also compute the multipoles of the correlation function as

$$\xi_{gg, 2\ell}(s) = \frac{2\ell + 1}{2} \int d\mu \xi_{gg}(s, \mu) L_{2\ell}(\mu) d\mu \quad (11)$$

where $s = \sqrt{r_p^2 + \Pi^2}$ is the separation between pair of galaxies in the redshift space and $\mu = \Pi/s$.

2.2.2 Modelling

The galaxy cross correlation function between samples S and D in redshift space is given by

$$\xi_{gg}(r_p, \Pi) = \int dz W(z) b_{g,S}(s, z) b_{g,D}(s, z) r_{gg}(s, z) \int \frac{d^2 k_{\perp} dk_z}{(2\pi)^3} \times P_{\delta\delta}(\vec{k}, z) (1 + \beta_S \mu_k^2) (1 + \beta_D \mu_k^2) e^{i(\vec{r}_p \cdot \vec{k}_{\perp} + \Pi k_z)}. \quad (12)$$

where $s = \sqrt{r_p^2 + \Pi^2}$, b_g is the galaxy bias and is in general a function of redshift and scale, $P_{\delta\delta}$ is the matter power spectrum. The Kaiser factor $(1 + \beta \mu_k^2)$ accounts for the effects of redshift space distortions (Kaiser et al. 1995) with $\beta = f(z)/b_g$, f is the growth function. We also introduced the cross correlation coefficient, $r_{gg}(s, z)$, between the two samples of galaxies but we will assume that $r_{gg}(s, z) = 1$ on all scales used for fitting the model ($r_p > 5h^{-1}\text{Mpc}$). $W(z)$ is the redshift weight accounting for the effective contributions from different redshifts to the measured correlation function and is given by (Mandelbaum et al. 2011)

$$W(z) = \frac{p(z)^2}{\chi^2(z) d\chi/dz} \left[\int \frac{p(z)^2}{\chi^2(z) d\chi/dz} dz \right]^{-1}. \quad (13)$$

$p(z)$ is the redshift probability distribution for the galaxy sample.

To compute the projected correlation function, we will assume a scale independent bias, b_g and use the effective redshift, z , for our sample computed by integrating over weights $W(z)$. We then integrate over the correlation function multipoles to obtain the projected correlation function as (Baldauf et al. 2010)

$$w_{gg}(r_p) = \sum_{\ell=0}^2 2 \int_0^{\Pi_{\max}} d\Pi \xi_{gg, 2\ell}(r) L_{2\ell}(\Pi/r) \quad (14)$$

where $L_{2\ell}$ are the Legendre polynomials, prefactor 2 arises because we assume symmetry around $\Pi = 0$ and change the limits of integration. $\xi_{gg, 2\ell}(r)$ are the correlation function multipole given as

$$\xi_{gg, 2\ell}(r) = (-1)^{\ell} \alpha_{2\ell}(\beta(z)) \frac{b_{g,S} b_{g,D}}{2\pi^2} \int dk k^2 P_{\delta\delta}(k) j_{2\ell}(kr) \quad (15)$$

where $j_{2\ell}$ are the spherical bessel functions. We use the package `mcfit` (Li et al. 2019) to compute the correlation function multipoles. The coefficients $\alpha_{2\ell}(\beta)$ are given by (Baldauf et al. 2010)

$$\alpha_0(\beta) = 1 + 1/3(\beta_S + \beta_D) + 1/5\beta_S\beta_D \quad (16)$$

$$\alpha_2(\beta) = 2/3(\beta_S + \beta_D) + 4/7\beta_S\beta_D \quad (17)$$

$$\alpha_4(\beta) = 8/35\beta_S\beta_D \quad (18)$$

2.3 Galaxy-FP residual cross correlations

2.3.1 Estimator

To compute the cross correlations between the galaxy density and the FP residuals, we use

$$\xi_{g\lambda}(r_p, \Pi) = \frac{\lambda_S D - \lambda_S R_D}{R_S R_D}, \quad (19)$$

λ_S is the FP residuals for sample S , D is the sample of galaxies used as galaxy density tracers and R_S, R_D are the corresponding randoms sample. $\lambda_S D$ effectively refers to the pair counts, weighted with FP residuals λ ,

$$\lambda_S D(r_p, \Pi) = \sum_{S,D} \lambda_S w_{SD}. \quad (20)$$

The $\sum_{S,D}$ is over all the galaxy pairs with separation within the (r_p, Π) bin limits, w_{SD} is the weight assigned to the pair of galaxies and λ_S is the FP residual from sample S . $S_\lambda R_D$ measures the same quantity with density tracer sample being replaced by the random points. Randoms subtraction can remove potential additive systematics that do not correlate with underlying galaxy density and also leads to optimal covariance (Singh et al. 2017).

We caution that this estimator can be biased if the $\langle \lambda \rangle$ is not zero, even after including the randoms subtraction. This is because the λ is estimated at the position of the galaxies and is hence weighted by the galaxy density field, which results in contribution from the galaxy clustering in case the $\langle \lambda \rangle$ is not zero, i.e.

$$\begin{aligned} \xi_{g\lambda}(r) &= \left\langle \left[(\lambda_0 + \langle \lambda \rangle) (1 + \delta_g^S) \right] \delta_g^D \right\rangle(r) \\ &= \left\langle \lambda_0 (1 + \delta_g^S) \delta_g^D \right\rangle(r) + \langle \lambda \rangle \left\langle \delta_g^S \delta_g^D \right\rangle(r) \end{aligned} \quad (21)$$

where we used λ_0 to explicitly define the mean zero quantity. Thus before computing the correlation function, we subtract out $\langle \lambda \rangle$ even though FP definition and our fitting procedure ensures that it is very small.

The projected correlation function $w_{g\lambda}$ is then obtained by integration over line of sight as in eq. (10) and the multipoles are obtained as in eq. (11).

2.3.2 Modelling

Following Hirata (2009), we assume that the deviations from fundamental plane are correlated with the tidal field due to the effects of intrinsic alignments of galaxy shapes, i.e. galaxy shapes are aligned with tidal field in the three dimensions and the projection effects then lead to correlations between tidal field and the projected shape and size of galaxies. Galaxy sizes are affected by the intrinsic alignments along the line of sight. λ can then be described in terms of matter field as

$$\lambda = -A_\lambda \zeta \left[\nabla_z \nabla_z \nabla^{-2} - \frac{1}{3} \right] \delta_m \quad (22)$$

$$\lambda = A_\lambda \zeta \left[\frac{1}{3} - \frac{k_z^2}{k^2} \right] \delta_m \quad (23)$$

$$\lambda = A_\lambda \zeta [1 - 3\mu^2] \delta_m \quad (24)$$

where we used $\zeta = \frac{C_1 \rho_{crit} \Omega_m}{D(z)}$ and $\mu_{\vec{k}} = k_z / \vec{k}$. Our sign convention implies that for $A_\lambda > 0$ galaxies in higher overdensities (larger δ_m) have larger size. Following convention of intrinsic alignments studies (eg. Joachimi et al. 2011), we will use $C_1 \rho_{crit} = 0.0134$.

We note here that in general it is plausible that additional galaxy environment effects also affect the projected galaxy sizes, in which case the deviations from the fundamental plane can be written in terms of the trace of the tidal

field, $\lambda \propto \nabla^2 \phi \propto \delta_m$. This formalism also results in the similar form for λ as in eq. (24), but with different constants and different line of sight anisotropy term as compared to $(1 - 3\mu^2)$. Such a model was assumed by Joachimi et al. (2015) when modeling λ . We will use the form in eq. (24) to fit the measurements of projected correlation functions (where line of sight anisotropy has negligible effect due to large line of sight integration) and study the deviations from the model by comparing A_λ to the amplitude of intrinsic alignments of galaxies A_{IA} , where the expectation under the model is $A_\lambda = A_{IA}/2$ (Hirata 2009). The primary difference between our model and that of Joachimi et al. (2015) is that fitted values of A_λ are rescaled by a constant $\zeta/3 = C_1 \rho_{crit} \Omega_m / 3D(z)$.

To check for the impact of the $(1 - 3\mu^2)$ term, we will also compute the multipole moments of the galaxy- λ cross correlations and we will replace this factor with $(1 + \beta_\lambda \mu^2)$, i.e.

$$\lambda = A_\lambda \frac{\zeta}{3} [1 + \beta_\lambda \mu^2] \delta_m \quad (25)$$

where β_λ is a free parameter to be fit, with fiducial value set to $\beta_\lambda = -3$.

The cross correlation function of λ with galaxies in redshift space is given by

$$\begin{aligned} \xi_{g\lambda}(r_p, \Pi) &= A_\lambda \frac{\zeta}{3} \int dz W(z) b_g(r, z) r_{cc}(r, z) \\ &\int \frac{d^2 k_\perp dk_z}{(2\pi)^3} P_{\delta\delta}(\vec{k}, z) (1 + \beta_g \mu_k^2) (1 + \beta_\lambda \mu_k^2) e^{i(\vec{r}_p \cdot \vec{k}_\perp + \Pi k_z)}, \end{aligned} \quad (26)$$

where $r_{cc}(r, z)$ is the cross correlation coefficient between galaxies and matter. In this work, we will assume $r_{cc}(r, z) = 1$ on the scales used to fit the model ($r_p > 5h^{-1}\text{Mpc}$). Note that Kaiser factor for RSD $(1 + \beta_\mu \mu_k^2)$ is different from the galaxy clustering as we assume that only galaxy positions are affected by RSD and λ carries the $(1 + \beta_\lambda \mu^2)$ term (we are ignoring the fact that the FP residuals are affected by RSD. RSD effects on λ scale as $\Delta\lambda \propto \frac{v}{H(z)D(z)}$, v is galaxy velocity and $D(z)$ is the line of sight distance to the galaxy).

The projected correlation function and multipoles are then computed using similar transforms as in galaxy clustering, eq. (14) and eq. (15). When computing the projected correlation function, $w_{g\lambda}$, we fix $\beta_\lambda = -3$, while when fitting the multipoles β_λ is a free parameter.

As shown in eq. (21), since the FP residuals are sampled at the position of the galaxies, the measured $\xi_{g\lambda} = \lambda_S (1 + \delta_g^S) \delta_g^D$ is weighted by the galaxy density and thus includes higher order terms (see Blazek et al. 2015, for detailed study of this effect in measurements of intrinsic alignments of galaxies). Detailed modeling of this effect is outside the scope of current work and we will ignore it in our models.

2.4 Galaxy-Intrinsic shear

We follow Singh et al. (2015) and Singh & Mandelbaum (2016) for the measurements and modeling of intrinsic alignments. We only briefly describe the methodology here and refer the reader to Singh et al. (2015) for more details.

2.4.1 Estimator

The cross correlations between galaxy shapes and the galaxy density field are measured as

$$\xi_{g+}(r_p, \Pi) = \frac{S_+D - S_+R_D}{R_S R_D}, \quad (27)$$

where S_+D refers to the summation over the radial shear, $\gamma_{+,S}$, measured in the coordinate frame defined by the pair of galaxies

$$S_+D = \sum_{S,D} \gamma_{+,S} w_{SD}. \quad (28)$$

where $\gamma_{+,S}$ is positive for radial alignment and negative for tangential alignments.

The projected correlation function w_{g+} is obtained by integration over line of sight as in eq. (10)

2.4.2 Modeling

We assume the nonlinear-alignment model (Hirata & Seljak 2003) for modeling the alignment signal

$$\xi_{g+}(r_p, \Pi) = A_I \zeta \int dz W(z) b_g(r, z) r_{cc}(r, z) \int \frac{d^2 k_\perp dk_z}{(2\pi)^3} \times P_{\delta\delta}(\vec{k}, z) (1 + \beta \mu_k^2) (1 - \mu_k^2) e^{i(\vec{r}_p \cdot \vec{k}_\perp + \Pi k_z)}, \quad (29)$$

with the line of sight anisotropy $1 - \mu_k^2$ accounting for the projection effects (see Singh & Mandelbaum 2016, for a detailed analysis). We will only use the projected correlation functions for intrinsic alignments where these terms have negligible effect.

2.5 Redshift-space galaxy power spectrum

The model for the galaxy power spectrum in redshift space is based on Hand et al. (2017b). We only briefly summarize the formalism here, referring the reader to Hand et al. (2017b) for more details.

In this model, we follow the halo model formalism in Okumura et al. (2015) and separately model the 1-halo (correlations of galaxies in the same halo) and 2-halo (correlations of galaxies in different halos) contributions to the clustering of galaxies. To achieve such modeling, it is convenient to decompose the galaxy density field in redshift space into contributions from centrals and satellites:

$$\delta_g(\mathbf{k}) = (1 - f_s) \delta_c(\mathbf{k}) + f_s \delta_s(\mathbf{k}), \quad (30)$$

where f_s is the satellite fraction, and δ_c and δ_s are the density field of centrals and satellites, respectively. The total galaxy power spectrum in redshift space, in turn, can be modelled as:

$$P_{gg}(\mathbf{k}) = (1 - f_s)^2 P_{cc}(\mathbf{k}) + 2f_s(1 - f_s) P_{cs}(\mathbf{k}) + f_s^2 P_{ss}(\mathbf{k}), \quad (31)$$

where P^{cc} , P^{cs} , and P^{ss} are the centrals auto power, central-satellite cross power, and satellite auto power, respectively. We then separate 1-halo and 2-halo terms by further decomposing the galaxy sample into the following four subsamples: centrals without satellites (denoted as “type A” centrals), centrals with satellites (“type B” centrals), satellites with no other satellites (“type A” satellites), and satellites with

other neighboring satellites (“type B” satellites). We also account for the Fingers-of-God (FoG) effect when modeling 1-halo and 2-halo terms in redshift space, by separately modeling the FoG effect from each subsample.

The model for the dark matter halo power spectrum in redshift space is based on the distribution function expansion (Seljak & McDonald 2011; Okumura et al. 2012b,a; Vlah et al. 2012; Vlah et al. 2013; Blazek et al. 2011), and Eulerian perturbation theory and halo biasing model is applied to model the halo velocity correlator terms (Vlah et al. 2013). The results of N-body simulations are also used to calibrate key terms in the model.

The resulting galaxy power spectrum model depends on 13 physically-motivated parameters, which include: the Alcock-Paczynski (AP) effect parameters $\alpha_{||}$, α_{\perp} , the growth rate f and the amplitude of matter fluctuations σ_8 evaluated at the effective redshift of the sample z_{eff} , the linear bias of the type A centrals and type A and B satellites [b_{1cA} , b_{1sA} , b_{1sB}], the satellite fraction f_s , the fraction of type B satellites f_{sB} , the mean number of satellite galaxies in halos with more than one satellite ($\langle N_{>1,s} \rangle$), the centrals FoG velocity dispersion σ_c , The type A satellites FoG velocity dispersion σ_{sA} , and normalization nuisance parameter for the 1-halo amplitude f_{sB}^{1h} . We follow the notations introduced in Hand et al. (2017b). In this work, we fix the AP parameters to their fiducial values, 1.

We measure the clustering of galaxies using the multipole moments of the power spectrum $P_l(k)$. In this work, we take the FFT-based algorithm presented in Hand et al. (2017a), built upon the methods proposed in Bianchi et al. (2015) and Scoccimarro (2015), and this allows fast evaluation of the estimator in Yamamoto et al. (2006). Using the spherical harmonic addition theorem to expand the Legendre polynomials into spherical harmonics, we write the multipole estimator as:

$$P_l(k) = \frac{2l+1}{A} \int \frac{d\Omega_k}{4\pi} F_0(\mathbf{k}) F_l(-\mathbf{k}), \quad (32)$$

where Ω_k is the solid angle in Fourier space, \mathcal{L}_l is the Legendre polynomial, w is the weight, A is the normalization defined as $A \equiv \int d\mathbf{r} [n(\mathbf{r})w(\mathbf{r})]^2$, and

$$F_l(\mathbf{k}) = \int d\mathbf{r} F(\mathbf{r}) e^{i\mathbf{k} \cdot \mathbf{r}} \mathcal{L}_l(\hat{\mathbf{k}} \cdot \hat{\mathbf{r}}) = \frac{4\pi}{2l+1} \sum_{m=-l}^l Y_{lm}(\hat{\mathbf{k}}) \int d\mathbf{r} F(\mathbf{r}) Y_{lm}^*(\hat{\mathbf{r}}) e^{i\mathbf{k} \cdot \mathbf{r}}. \quad (33)$$

The weighted galaxy density field $F(\mathbf{r})$ is given by

$$F(\mathbf{r}) = \frac{w(\mathbf{r})}{A^{1/2}} [n(\mathbf{r}) - \alpha n_s(\mathbf{r})], \quad (34)$$

where n and n_s are the number density field for the galaxy and randoms catalogs respectively, and the factor α normalizes n_s to n .

2.5.1 IA effects on RSD

To account for the effects of intrinsic alignments of galaxies on the selection functions of galaxies and hence the RSD measurements, we follow the formalism in Hirata (2009);

Martens et al. (2018), defining the bias in observed galaxy density as:

$$\hat{\delta}_g(\mathbf{x}, \lambda) = \delta_g(\mathbf{x}) + \epsilon(\lambda(\mathbf{x})) \quad (35)$$

To derive the error ϵ , we assume that the probability of a galaxy in the observed sample, O , is given as

$$P(O|T, \lambda) = P(T)P(\lambda)(1 + S(\lambda)) \quad (36)$$

Where T is the target sample, λ is the FP residual for the given galaxy and $S(\lambda)$ is the size dependent selection function. We can also write the number of galaxies with the observed value of λ as

$$N_\lambda = \frac{dN}{d\lambda} = NP(\lambda)(1 + S(\lambda)), \quad (37)$$

N is the total number of galaxies. Following the ansatz in Hirata (2009); Martens et al. (2018), we assume that the some galaxies are missed when they are aligned with the plane of the sky, i.e. have positive λ . Under this assumption and assuming that the intrinsic distribution λ is symmetric within T , we can write

$$S(\lambda) = \frac{N_\lambda - N_{-\lambda}}{N_\lambda + N_{-\lambda}} \quad (38)$$

where $N_{-\lambda}$ is the number of galaxies with a negative value of λ . Note that the mean of $S(\lambda)$ is zero by construction. $S(\lambda)$ is also zero if there are no size dependent selection effects, since we assume the λ distribution to be symmetric ($N_\lambda = N_{-\lambda}$ when no size dependent selection).

Galaxies have some random λ values, λ_R , due to intrinsic variations in galaxy properties as well as random projections. The additional λ_I sourced by intrinsic alignments acts as a small perturbation on top of the λ_R (we assume $\lambda_I \ll \lambda_R$). We can then write the error ϵ that is relevant for cosmological inferences as

$$\epsilon(\lambda_R(\mathbf{x}) + \lambda_I(\mathbf{x})) = S(\lambda_R) + \lambda_I \frac{\partial S(\lambda)}{\partial \lambda} \Big|_{\lambda=\lambda_R} \quad (39)$$

Since λ_R and hence $S(\lambda_R)$ does not correlate with the density field, the relevant part of ϵ that correlates with the density field can be written as

$$\epsilon(\mathbf{x}) \approx \gamma A_\lambda \zeta \left[\frac{1}{3} - \mu^2 \right] \delta_m(\mathbf{x}) \quad (40)$$

where we used the relation of λ to tidal field as defined in eq. (24) and defined the ensemble response γ as

$$\gamma = \left\langle \frac{\partial S(\lambda)}{\partial \lambda} \right\rangle = \frac{1}{\int d\lambda N_\lambda} \int d\lambda N_\lambda \frac{\partial S(\lambda)}{\partial \lambda} \quad (41)$$

The error in the growth rate and galaxy bias measurements is given by

$$\Delta f = \hat{f} - f_0 = -\gamma A_\lambda \zeta \quad (42)$$

$$\hat{b}_g = b_{g,0} + \frac{1}{3} \gamma A_\lambda \zeta = b_{g,0} - \frac{1}{3} \Delta f \quad (43)$$

We will determine γ from the distribution of FP residuals. We note that since the datasets we will be using are already affected by the selection effects, $S(\lambda)$, this can introduce a bias the estimations of the γ (the mean of λ distribution is shifted which biases S). We will work under the assumption that the selection effects are small and hence the shift in the mean of the distribution and the bias in γ is also small. A_λ

will be determined using the cross correlations between the FP residuals and the galaxy density field and ζ is a cosmology dependent constant. We will also compute the variations in f and b from our RSD analysis and these measurements will allow us to test the eq. (42) and eq. (43).

In section 4.3.1, we will also split the galaxy sample into two subsamples according to the sign of FP residuals, following Martens et al. (2018). These subsamples are expected to have almost identical γ values: $\gamma^+ \approx \gamma^-$, where $+$ and $-$ indicates samples with positive and negative FP residuals, respectively. That is because $\partial S(\lambda)/\partial \lambda$ is mirrored across the y-axis, as shown in figure A1. Therefore, we expect that the growth rate measurements between the two FP residual subsamples is consistent: $\Delta f^+ - \Delta f^- = -(\gamma^+ - \gamma^-) A_\lambda \zeta \approx 0$, unlike the model assumed by Martens et al. (2018).

2.6 Covariance matrices

For the correlation function measurements, we compute the covariance matrices using Jackknife resampling method by splitting the sample into 100 approximately equal area patches (68 patches in North Galactic Cap (NGC) and 32 in South Galactic Cap (SGC) of BOSS data described in section 3). Since the jackknife covariances are noisy, leading to biased inverse matrix, we also apply the Hartlap correction (Hartlap et al. 2007) when computing the inverse covariance matrix used in the likelihood functions.

For the multipoles in Fourier space, we assume the theoretical Gaussian covariance, following Grieb et al. (2016b):

$$C_{\ell_1 \ell_2}(k_i, k_j) = \frac{2(2\pi)^4}{V_{k_i}^2} \delta_{ij} \int_{k_i - \Delta k/2}^{k_i + \Delta k/2} \sigma_{\ell_1 \ell_2}^2(k) k^2 dk, \quad (44)$$

where $V_{k_i} = 4\pi[(k_i + \Delta k/2)^3 - (k_i - \Delta k/2)^3]/3$ is the volume of the shell in k -space. When the expected mean number density $\bar{n}(z)$ is varying, the per-mode covariance $\sigma_{\ell_1 \ell_2}^2(k)$ is given by Yamamoto et al. (2006):

$$\sigma_{\ell_1 \ell_2}^2(k) = \frac{(2\ell_1 + 1)(2\ell_2 + 1)}{A^2} \int_{-1}^1 d\mu \int_{V_s} d\mathbf{r} \bar{n}^4(\mathbf{r}) w^4(\mathbf{r}) [P(k, \mu, z) + \bar{n}^{-1}(\mathbf{r})]^2 \mathcal{L}_{\ell_1}(\mu) \mathcal{L}_{\ell_2}(\mu), \quad (45)$$

where the normalization terms A is defined as $A \equiv \int d\mathbf{r} [\bar{n}(\mathbf{r}) w(\mathbf{r})]^2$, following the notations in section 2.5.

For the galaxy subsamples we define in section 3, we compute their mean number densities in order to obtain correct covariance matrices using eq. 44.

3 DATA

In this work we use the LOWZ ($0.16 < z < 0.43$) and CMASS ($0.43 < z < 0.7$) spectroscopic samples from SDSS-III BOSS (Blanton et al. 2003; Bolton et al. 2012; Ahn et al. 2012; Dawson et al. 2013; Smee et al. 2013) data release 12 (DR12; Alam et al. 2015), which are selected using the imaging data from SDSS-I and SDSS-II surveys. The SDSS survey (Gunn et al. 1998; York et al. 2000; Hogg et al. 2001; Ivezić et al. 2004; Fukugita et al. 1996; Smith et al. 2002; Eisenstein et al. 2001; Gunn et al. 2006; Richards et al. 2002; Strauss et al. 2002) (Lupton et al. 2001; Pier et al. 2003;

Tucker et al. 2006; Abazajian et al. 2009; Aihara et al. 2011; Padmanabhan et al. 2008). To fit the FP, we also obtain the photometric measurements for our galaxies, specifically the Radii, axis ratios and magnitudes from de Vaucouleurs fits from the SDSS photometric catalog. The magnitudes are corrected for the extinction and we also apply k-corrections using the formalism of Wake et al. (2006).

When computing galaxy clustering and galaxy-FP cross correlations, we apply weights to the galaxies, where the weights are given by (Ross et al. 2012)

$$w = w_{\text{sys}}(w_{\text{no-z}} + w_{\text{cp}} - 1), \quad (46)$$

where w_{sys} weights correct for the variations in the selection function on the sky (important for CMASS) and $w_{\text{no-z}}$, w_{cp} correct for missing redshifts due to failure to obtain redshift (no-z) or fiber collisions for close pairs, cp .

For intrinsic alignments of galaxies, the shape sample used to estimate the shear is described in more detail in Reyes et al. (2012) and Singh et al. (2015).

Furthermore, to study the dependence of FP and residuals on galaxy properties, we also split the BOSS samples based on color and luminosity. We follow the procedure from Singh et al. (2015), whereby we split the samples in narrow redshift bins based on the percentiles of the color and luminosity. We make 5 color samples, $C_1 - C_5$, with each subsample containing 20% of the galaxies such that C_1 starts with reddest galaxies and the subsequent samples contain progressively bluer galaxies. Split in the redshift bins ensures that each sample has the same redshift distribution. We follow the similar procedure for luminosity and make 4 luminosity subsamples, $L_1 - L_4$ with L_1 being brightest and L_4 being faintest. $L_1 - L_3$ contain 20% of the sample each while L_4 contains 40% of galaxies.

For the LOWZ sample, we also identify the galaxies in groups using the counts-in-cylinders technique (Reid & Spergel 2009) using the same procedure as was followed in Singh et al. (2015). Galaxies that are not in groups (or are in group of 1) are designated as ‘Field’ galaxies, the brightest galaxy in a group of more than 1 galaxy is designated as BGG (brightest group galaxy) while all non-BGG galaxies are designated as satellite galaxies.

Since we are splitting the samples by color, luminosity and also FP residuals, the variations in the photometry across the sky can lead to some variations in selection function of the galaxies for these sub-samples. The variations can introduce biases when computing the galaxy auto correlation functions for these galaxies. To avoid this issue, we will use cross correlations when computing the correlation functions, where we cross correlate the sub-samples with the full sample from which they were selected. As a result the biases in the signal are reduced though the covariance will still be affected (Singh et al. 2017). In the power spectrum measurements, we will use the auto correlations. To reduce the impact of selection functions on sub samples, we reweight the randoms provided by BOSS to correspond to these samples. We compute the weight using the ratio of number galaxies within the sub-samples to number of galaxies in the full sample, within each $\sim 80 \text{ deg}^2$ patch we generated for the jackknife calculations. We also tried the weights computed in much smaller patches, but those weights biased the measurements on small scales. More details of randoms re-weighting are presented in the appendix E1.

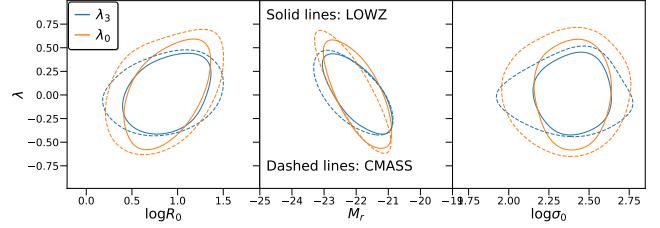


Figure 1. The residuals over the FP for standard FP, λ_0 and the redshift dependent FP λ_3 as function of galaxy size, R_0 , r band magnitude M_r , and the velocity dispersion σ_0 . We show the contours covering 95% of the sample for both LOWZ (solid lines) and CMASS (dashed lines) samples.

4 RESULTS

In this section we present our results, beginning with the fits of FP to LOWZ and CMASS as well as various subsamples and analysis of FP residuals based on some galaxy properties. Then we present the measurements of cross correlations between FP residuals and galaxy density and comparison of these cross correlations with the Intrinsic alignments of galaxies. Following this we present the measurements of redshift space distortions (RSD) and the correlations between RSD constraints and FP residuals. Some additional details, analysis, and tests based on systematics are presented in the appendices of the paper.

4.1 FP Fits

In this section we present results of fitting FP to full LOWZ and CMASS samples and an analysis of the FP residuals based on the redshift, luminosity and environment of the galaxies. Note that unless mentioned otherwise, in this subsection, FP residuals are obtained from fitting FP to the full samples and not the sub-samples.

In figure 1, we show the contour plots of the FP residuals as function of galaxy size, magnitude and velocity dispersion. For the standard FP, λ , we obtain the RMS values of $\lambda_{\text{rms}} = 0.22$ for LOWZ and $\lambda_{\text{rms}} = 0.26$ for CMASS sample and for the redshift dependent FP, λ_3 , we obtain $\lambda_{\text{rms}} = 0.15$ for LOWZ and $\lambda_{\text{rms}} = 0.16$ for CMASS samples. Note that λ is defined in \log_e (ln) base and hence λ_{rms} is larger than the scatter in $\log_{10} R$ space by a factor of $\ln 10 \sim 2.3$. After accounting for this effect, our results are consistent with the FP scatter of ~ 0.1 obtained by Saulder et al. (2019); Joachimi et al. (2015), albeit for somewhat different samples.

Also note in figure 1 that the FP residuals are correlated with the galaxy properties. We now investigate some of these correlations in more detail.

4.1.1 Redshift dependence

In figure 2a we present the redshift dependence of the mean and the RMS of the FP residuals for both LOWZ and CMASS samples. For the standard FP we find a strong correlation of the mean residuals, λ_0 , with the redshift. Including redshift dependence within the FP using polynomials reduces the dependence of the mean by a large magnitude and also reduces the RMS (as function of z) by $\sim 10\%$.

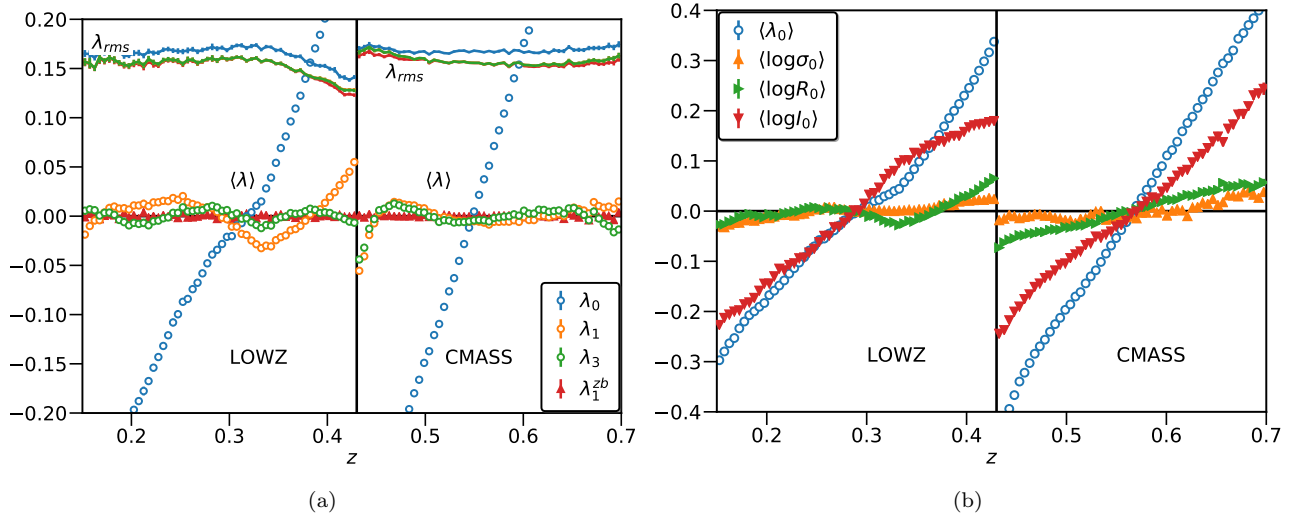


Figure 2. a) Redshift dependence of the mean and standard deviation (mean subtracted RMS) of the FP residuals for both LOWZ and CMASS samples. The subscript, λ_i , $i \in [0, 1, 3]$ denotes the order of the polynomial in z used for fitting FP. The superscript ‘ zb ’ denotes the sample fitted in narrow redshift bins $\Delta z = 0.02$. The residuals over for the standard fundamental plane, λ_0 , have strong dependence on the redshift and including redshift polynomials in the FP reduce this dependence as well as the scatter. Fitting FP within small redshifts further reduces the mean of FP (though there can be evolution within the bins). b) Redshift evolution of galaxy properties that are included in the FP. The redshift dependence of the residuals for standard FP can be explained by the redshift dependence of these properties, especially the surface brightness of galaxies, $\log I$, which has the strong and monotonic dependence on redshift, driven by the $\log(1+z)$ correction for the Tolman dimming.

The change (reduction) in the mean is largest when using the first order polynomial with some further improvement when going to the third order polynomial. There are still small residuals correlations between the mean and redshift and such correlations can potentially be important for the correlation functions we present in section 4.2 and for the cosmological applications of the FP in general. To further reduce correlation between mean and the redshift, we instead fit the FP in narrow redshift bins, $\Delta z = 0.02$ (this choice is motivated to keep the bin size small but have large enough line of sight size so as to not bias the cross correlation measurements presented in section 4.2). Fits in the bins further reduce the impact of the redshift dependent residuals. We will use λ_3 as our fiducial FP (unbinned with third order polynomial in redshift), but we will test the cross correlation results with the binned FP for comparison.

To study the source of the redshift dependence of FP, we show the redshift dependence of the galaxy properties in figure 2b. The velocity dispersion and physical radius only have mild dependence on redshift for both LOWZ and CMASS sample. The surface brightness of the galaxies on the other hand evolves strongly with redshift and is the primary driver for the redshift evolution of the standard FP residuals, λ_0 . The redshift evolution of surface brightness is driven by redshift dimming (Tolman 1930) of the surface brightness, as a result of which we only observe galaxies with larger surface brightness at higher redshifts. The evolution of surface brightness is very similar to the $\log(1+z)$ correction that was included in the eq. 4. Hence, when including the redshift polynomials into the FP, we are essentially undoing the $\log(1+z)$ correction. Including $\log(1+z)$ dependence in the FP is also a possibility instead of the polynomials in z , but we opt for the polynomials (or fit in narrow z bins) as they provide extra degrees of freedom which can account

for the small redshift dependence of the velocity dispersion, physical radius and luminosity.

Our results on the redshift dependence of the FP are qualitatively consistent with those from Joachimi et al. (2015), where such trends were observed for the SDSS main galaxy sample. Due to the differences in the samples used in this study and Joachimi et al. (2015), a more quantitative comparison is difficult but we have tested our pipelines on the samples used in Joachimi et al. (2015) and we are able to reproduce their results.

4.1.2 Luminosity and environment dependence

In figure 3a, we show the dependence of the FP residuals on the environment as function of redshift. As in Joachimi et al. (2015), we observe that the brightest group galaxies, *BGGs* have positive residuals on average (they are larger in size than predicted by FP) while satellites have negative residuals implying they are smaller than average. It is tempting to interpret these results based on the environment dependence of galaxies, whereby centrals or *BGGs* tend to be larger but less concentrated while satellites under going tidal stripping tend to be smaller and more concentrated. However, in figure 3b we observe that the FP residuals are strongly correlated with the galaxy luminosity, where brighter galaxies have larger (or more positive) residuals. These trends can explain most of the variations between different galaxy types in figure 3a, with *BGGs* (satellites) being only marginally larger (smaller) after accounting for the luminosity evolution, as shown in the lower panel of figure 3b.

Given that $\lambda \propto -b \log I \propto b M_r$ (b is negative), the luminosity dependence of FP residuals λ is expected in case the various galaxy properties, namely luminosity, radius and velocity dispersion are not perfectly correlated in a way to

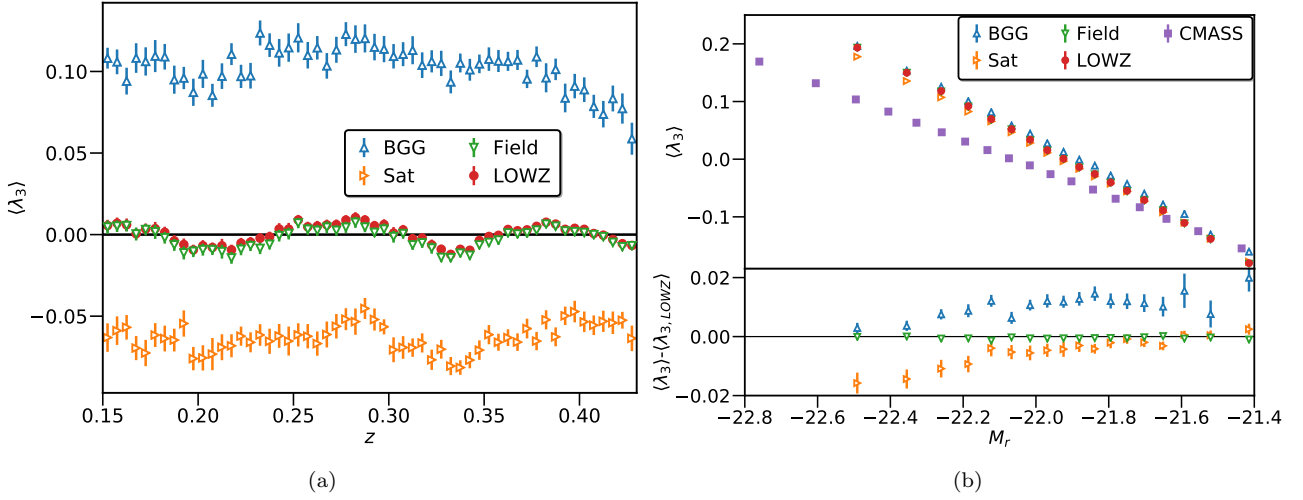


Figure 3. a) Dependence of the FP residuals on galaxy types. Similar to Joachimi et al. (2015), we observe that Brightest group galaxies (BGG), satellites and field galaxies have different FP residuals, with BGGs being larger than FP predictions while satellites being smaller. b) Mean FP residuals as function of the r band magnitude. Different types of galaxies, BGGs, Satellites, Field, all give very similar relation which suggests that the dependence in a) can be explained largely by magnitude (or luminosity) dependence of the FP residuals. In the lower panel we show the difference in the mean FP residuals of different samples relative to the full LOWZ sample. BGGs (satellites) are still higher (lower) than the full sample, though the differences are much smaller than in a). We do not observe any significant dependence of RMS of λ with luminosity.

cancel such a dependence. While it is possible to include the higher order luminosity dependence in the FP as well, we opt not to do so as FP residuals are correlated with multiple galaxy properties and systematics (see appendices) and including dependence on too many variables complicates the interpretation of FP and its residuals (inclusion of z -dependence is necessary to avoid biases in cross correlation measurements presented in section 4.2). Instead, we split our sample based on luminosity, color and environment as described in section 3 and fit the FP separately to those subsamples when studying the dependence of cross correlations on these galaxy properties.

4.2 Cross correlations with galaxy density

In this section we present the measurements of galaxy clustering and cross correlations between the galaxy positions and FP residuals. Throughout this section we will use FP with third order polynomial as the primary FP and when considering the subsamples, we will fit FP to each of the subsamples separately.

We begin by presenting the measurements of projected correlation functions using full LOWZ and CMASS samples in figure 4, with FP fit to the whole sample, λ_3 , FP fit in narrow redshift bins, $\lambda_{3,zb}$ and the FP without velocity dispersion, λ_3^f . We fit the models described in section 2 to both galaxy clustering and galaxy- λ cross correlations in the range $5 < r_p < 30 h^{-1} \text{Mpc}$. We do not fit the scales below $r_p < 5 h^{-1} \text{Mpc}$ as our model with assumption of linear bias is not expected to work well on these non-linear scales and we also do not use $r_p > 30 h^{-1} \text{Mpc}$, as there is some evidence of systematics in the galaxy- λ cross correlations (see also appendix E). We have checked that including scales between $30 < r_p < 70 h^{-1} \text{Mpc}$ does not significantly change the best fit parameters as measurements on those scales are

correlated and also have lower signal to noise compared to smaller scales.

For LOWZ sample, we obtain the linear galaxy bias, $b_g = 1.868 \pm 0.025$ and for CMASS sample we obtain $b_g = 2.096 \pm 0.019$. Using galaxy- λ_3 cross correlations, we obtain $A_\lambda = 5.8 \pm 1.6$ for LOWZ sample and $A_\lambda = 5.3 \pm 1.3$ for CMASS sample, with CMASS sample have lower noise due to larger volume of the sample, even though λ_{rms} is larger for CMASS sample. The values of A_λ do not change significantly if we fit FP in narrow redshift bins ($\lambda_{3,zb}$ in figure 4) and/or if we fit the FP for North and South regions of BOSS separately (measurements not shown). However, fitting the FP without velocity dispersion, λ_3^f , leads to significantly larger amplitude, with A_λ being larger by factor of $\sim 2-5$ depending upon the sample and the FP definition.

To understand the source of the correlations, in figure 5 we show the cross correlations of galaxy properties, the surface brightness $\log I$, physical radius, $\log R$ (orange) and velocity dispersion, $\log v$ in figure 5. The surface brightness shows strong correlations with the density field, with a large fraction of the signal driven by its strong evolution with redshift. These correlations provide interesting insights that the larger galaxies and ones with higher velocity dispersion tend to reside in the over dense regions but galaxies in over dense regions tend to have lower surface brightness.

The impact of these parameters can be observed in the lower panel of figure 5. The correlations of the FP residuals, λ , are essentially the weighted sum of the correlations of the galaxy properties, where the weights are the parameters of the FP. For λ_0 , surface brightness dominates given that the redshift evolution has not been corrected for and leads to large negative correlations. Once redshift evolution is corrected, the correlations of surface brightness decrease and hence the FP cross correlations become positive for λ_1 and λ_3 . This further justifies our choice to include the redshift evolution in the FP, as the correlation functions otherwise

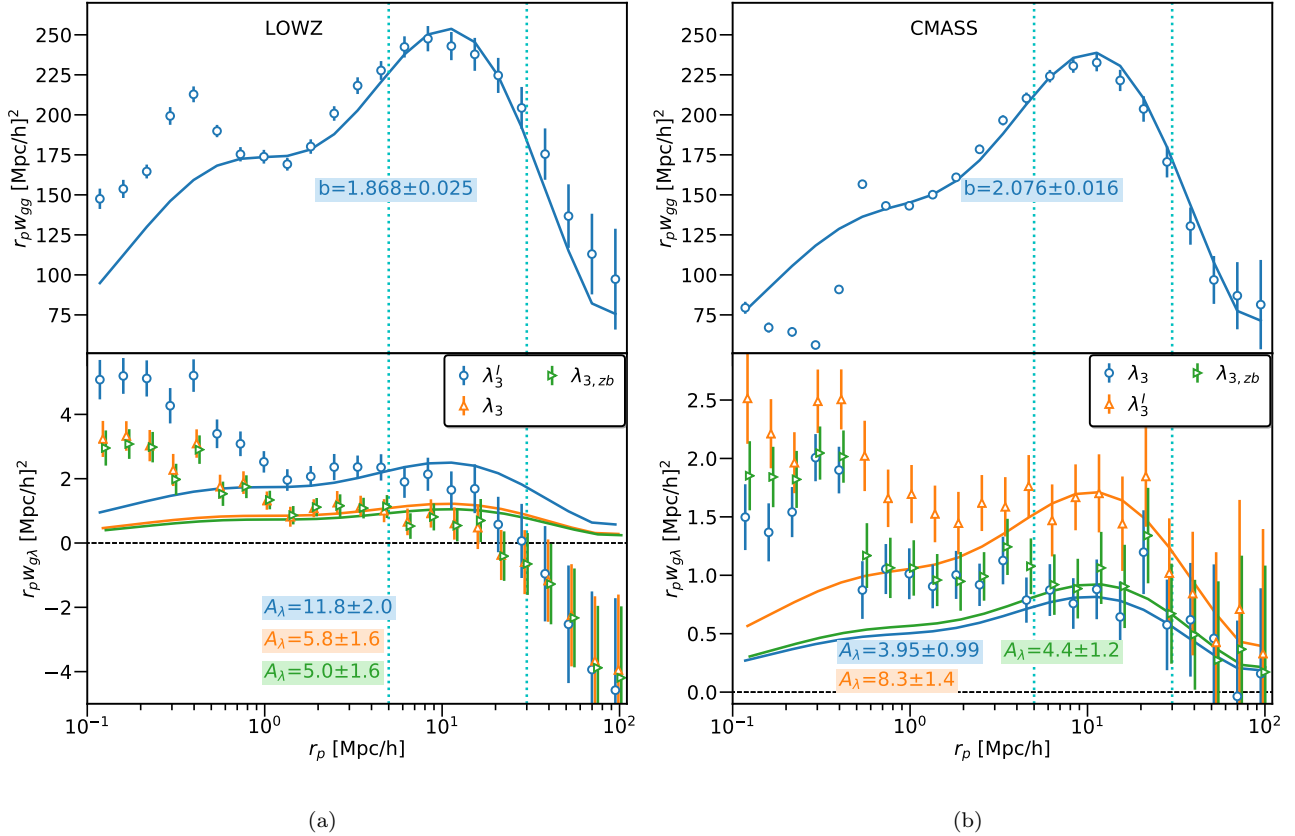


Figure 4. Measurements of galaxy clustering (upper panels) and galaxy- λ (lower panels) cross correlation functions for (a) LOWZ and (b) CMASS samples. Lower panel shows measurements with three different FP definitions, λ_3^I (blue, FP without velocity dispersion), λ_3 (orange) and FP fitted in z -bins $\lambda_{3,zb}$. We measure strong correlations between galaxies and FP residuals for both CMASS and LOWZ samples, with λ_3^I signal being factor of ~ 2 larger than the λ_3 . Given that the mean of λ_3^I and λ_3 are very similar and λ_3^I rms is larger by $\sim 10\%$, this difference is originating from the intrinsic differences between the two FP planes. Also, the consistency between λ_3 and $\lambda_{3,zb}$ suggests that the negative signal in LOWZ at large scales is unlikely due to any redshift dependent additive systematics in the FP (as observed in figure 1). Numbers quoted in the plots are the best fit galaxy bias and λ amplitude A_λ obtained by fitting the model in range $5 < r_p < 30 h^{-1} \text{Mpc}$ (marked by vertical dashed cyan lines). For the LOWZ sample, the $\chi^2_{\text{dof}} \sim 0.7$, even though the fit looks inconsistent with the data. This is due to strong correlations between the bins on large scales, likely driven by systematics (see also appendix E).

are dominated by the redshift evolution of the FP which itself is dominated by the redshift evolution of the surface brightness.

We also note that our measurements of galaxy- λ_3 cross correlations are not consistent with the results of Joachimi et al. (2015). This is because of the very different samples used in the two studies. As observed in section 4.1.2, the FP residuals are strongly correlated with the galaxy luminosity, with fainter galaxies correlating negative λ . As we will show in the appendix C, fainter sub-samples also show negative correlations between FP residuals and density, in our measurement. Given that SDSS main sample used in Joachimi et al. (2015) was fainter than BOSS samples, we hypothesize that the different measurements in the two studies are primarily due to the different galaxy samples. In order to rule out pipeline differences, we also reanalyzed the data of Joachimi et al. (2015) with our current pipeline and reproduced their results¹ (not shown).

4.2.1 Environment dependence

In figure 6, we show the correlations of FP residuals for group galaxies (satellites and BGGs) as well as the field galaxies. Satellites and BGGs have higher galaxy bias as expected since they are on average in more massive halos and hence more dense environments. More interestingly, FP residuals for both satellites and BGGs show much stronger correlations with the density field as compared to the field galaxies.

A_λ is rather large and also very similar for both Satellites and BGGs though the uncertainties for both samples are also large. Primary concern with such large signal is that since these galaxies reside in crowded regions, there can be some residual systematics in the photometry leading to such correlations. Since we subtract the randoms signal, additive systematics are unlikely to be able to lead to such large signals unless they strongly correlate with the galaxy density field. We have some evidence for systematics affecting the measurements, especially for LOWZ sample, but those systematics are predominately on large scales and do not lead to such large and significant A_λ values (see appendix E).

¹ Both pipelines were developed by S. Singh

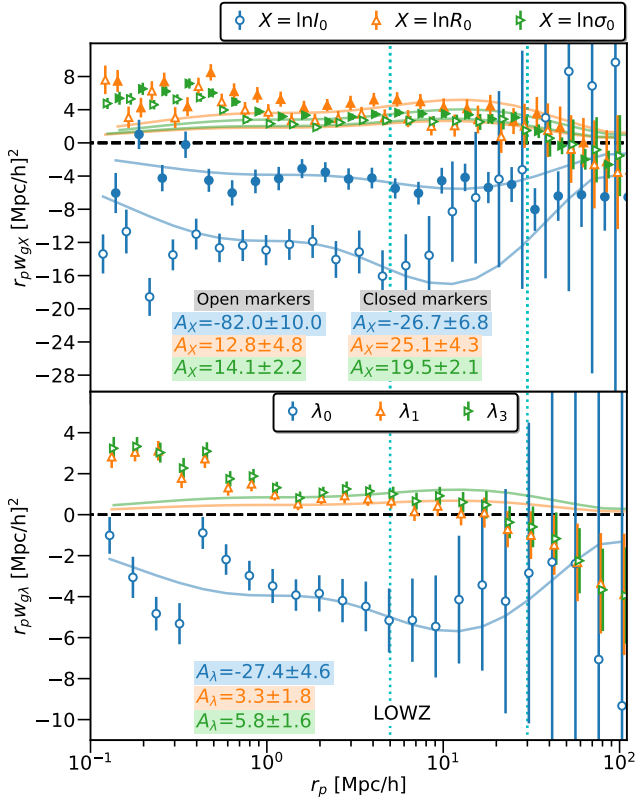


Figure 5. Upper panel: Galaxy- λ like cross correlation functions, where λ is replaced with different galaxy properties, namely the surface brightness, $\log I$ (blue), physical radius, $\log R$ (orange) and velocity dispersion, $\log v$ (green). For the open points, we set the mean of these galaxy properties to be zero only at the level of full sample, while for the closed points, the mean is set to zero within small redshift bins, $\Delta z = 0.02$. Size and velocity dispersion are positively correlated with the density field, though surface brightness shows negative correlations which are also stronger when redshift evolution is not corrected for. Lower panel: Cross correlation measurements using residuals from different definitions of fundamental plane. Standard FP residuals, λ_0 is negatively correlated driven by the effects of surface brightness, while FP corrected for redshift evolution show positive correlations with density.

We have also tested for the flags in SDSS photometry for blending and other photometry issues and BGGs, satellites and field galaxies all have very similar (low) rate of problematic photometry flags. Thus it is unlikely that satellite and BGGs results in particular are affected by the photometry problems.

Another possible explanations for such similarities is that the galaxy environment plays a strong role in determining the galaxy size, in addition to galaxy properties such as luminosity and size. To further study the impact of the environment on FP residuals, in figure 7 we show the A_λ as function of galaxy bias, b_g , where bias is a proxy for the galaxy environment (measurements for samples based on luminosity and color are presented in appendix C). Though there is considerable scatter, we observe that the galaxies with larger bias, i.e., the galaxies in over dense regions, tend to have larger A_λ . The observed high A_λ for satellite galaxies is consistent with this trend as these galaxies also have

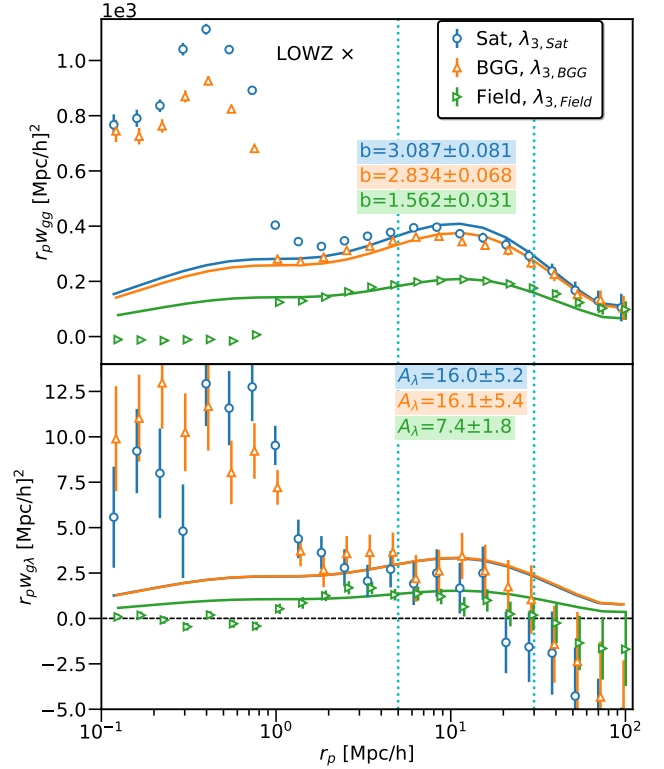


Figure 6. Galaxy clustering (cross correlation with LOWZ) and galaxy- λ cross correlation measurements for different environment samples, with full LOWZ sample as density tracers. Group galaxies, BGGs and Satellites, have similar clustering and galaxy-size cross correlations, unlike intrinsic alignments, where satellites do not show large scale shape alignments.

higher bias. These results are not straight forward to interpret within the context of the tidal stripping of satellite galaxies as was used as an explanation in Joachimi et al. (2015). Our results in figure 3b suggests that FP residuals of the satellite galaxies can primarily be explained by the luminosity dependence of the FP. However, when computing the correlation functions, we fit FP only to the satellite galaxies and within the satellite sample it is possible that stronger tidal stripping in denser environment can imprint some environment dependence on FP residuals leading to stronger correlations. In either case, our results suggest that environment plays a dominant role in determining the FP residuals of a galaxy. More detailed interpretation of these results will require a study using the realistic galaxy simulations to understand the relative importance of various processes involved in determining the galaxy sizes. We leave such a study for the future work.

4.2.2 Correlations with IA

As discussed in section 2, intrinsic alignments (IA) of galaxies coupled with the projection effects can lead to the scatter over the FP and the correlations between the FP residuals and the density field. The model in used in fitting the cross correlations between the FP residuals and the galaxy density field accounts for this effects and indeed if IA is the only cause of correlations of FP residuals, we expect $A_\lambda \sim A_I/2$.

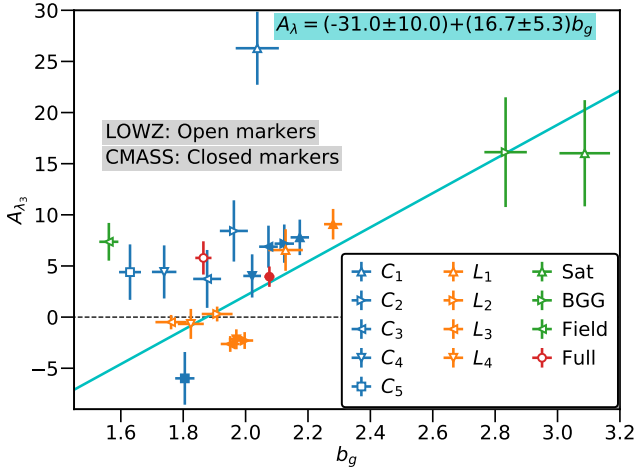


Figure 7. Environment dependence (as characterized by linear galaxy bias) of FP residuals. In more biased (overdense) environments, scatter about FP has stronger correlations with the environment.

In figure 8 we present the comparison of the intrinsic alignments amplitude (a detailed analysis of IA measurements was presented in Singh et al. (2015)) and in this work we repeat those measurements using BOSS DR12 data) and the FP residual amplitude A_λ derived from the cross correlations with the density field. For both LOWZ and CMASS samples we observe positive correlations between A_I and A_λ , samples with stronger IA also showing stronger correlations for FP. This is also consistent with the observations that IA and FP correlations have similar environment dependence (see previous section and Singh et al. (2015)). However, our measurements are inconsistent with the model predictions of $A_\lambda = A_{IA}/2$. In addition to considerable scatter in the measurements, the best fit linear models we obtained (not shown) deviated significantly from the model.

Our results suggest that the galaxy size correlation (as measured by FP) include contributions beyond the effects of intrinsic alignments and the projection effects. These contributions can come from physical processes such as stronger feedback in over dense regions or observational systematics affecting the estimation of size, magnitude and velocity dispersions of galaxies (eg. errors in PSF modeling, small fiber size used in spectroscopic measurements). The interpretation of these results is further complicated by the fact that IA also depends on the shape measurement methods. As shown in (Singh & Mandelbaum 2016), de Vaucouleurs shape results in $\sim 15 - 20\%$ larger IA amplitude though de Vaucouleurs shapes were also shown to be affected by systematics in the same study because of which we use the re-gaussianization shapes to measure the IA in this paper. Hence, it is difficult to fully explain the origin and the magnitude of the size correlation amplitudes and a detailed exploration of the physical origin of these effects will require further study with realistic simulations.

4.2.3 Multipoles

In figure 9 we show the measurements of the multipoles of the galaxy clustering and galaxy-FP cross correlation measurements. The monopole and quadrupole of the galaxy clus-

tering are consistent with the expectations from the redshift space distortion measurements. Here we fit the simple Kaiser model to fit both the monopole and quadrupole moments and we will present more detailed analysis of galaxy clustering multipoles in the next section. The galaxy bias obtained from these fits is consistent with the values obtained from the projected correlation functions. Since the model does not include the effects of non-linear corrections, it does not fit data well on small scales and hence we only use $30 < s < 70 h^{-1} \text{Mpc}$ to fit the galaxy-galaxy correlation functions and we further fix the growth rate to the value expected from our fiducial cosmology $f = 0.665(0.77)$ for LOWZ (CMASS). Since our focus in this section is to study the anisotropy of the galaxy-FP correlation function, we prefer to use a simpler model with few parameters over a more detailed RSD model presented in the next section.

In the lower panel, we present the measurements and the fits for the galaxy-FP cross correlation function. We detect both the monopole and the quadrupole moments of the correlation functions, pointing to significant line of sight anisotropy in these measurements. Some level of anisotropy is expected as the galaxy positions are measured in redshift space and the FP residuals are weighted with galaxy density field in the redshift space. To estimate the anisotropy contributions from the FP residuals, we fit for the anisotropy factor, β_λ (see eq. (25)) (galaxy anisotropy β_g is obtained from clustering). The best fit values of β_λ we obtain are consistent with zero, contrary to the expectations from the model which predicts $\beta_\lambda = -3$ ($\beta_\lambda = -3$ predicts positive quadrupole moments at large scales). These conclusions are not changed even if we fit with growth rate f as a free parameter, if we vary the minimum scale used in the fits ($r_{p,\min} = 20$ or $40 h^{-1} \text{Mpc}$) and even if we include the hexadecapole measurements.

While our measurements appear to rule out the influence of IA on the FP residuals, we note here that this is only true within the model we assumed in this work. Both IA and FP residuals are also weighted by the galaxy density field, which is measured in the redshift space and introduces higher order terms which can have significant contributions to the measured correlation functions. Furthermore, these higher order terms also contain the line of sight anisotropy terms which can in principle affect the β_λ constraints. Modeling these higher order terms accurately is out of the scope of this work and can be attempted in a future work.

4.3 IA effects on RSD

In this section we present the measurements of the galaxy power spectrum multipoles in Fourier space. In figure 10, we show the measured monopole $P_0(k)$, quadrupole $P_2(k)$, and hexadecapole $P_4(k)$ of the LOWZ NGC and CMASS NGC galaxies, using the FFT-based galaxy power spectrum estimator described in section 2.5. We then fit the RSD model presented in section 2.5 to the measured multipoles and find that the power spectrum multipoles are accurately modeled, down to scales of $k = 0.4 h \text{Mpc}^{-1}$, in agreement with Hand et al. (2017b). The fits to the SGC galaxies are not shown in the figure, but we also find a good agreement between the model and the SGC samples. We include the hexadecapole $P_4(k)$ because this improves RSD constraints significantly, as reported ear-

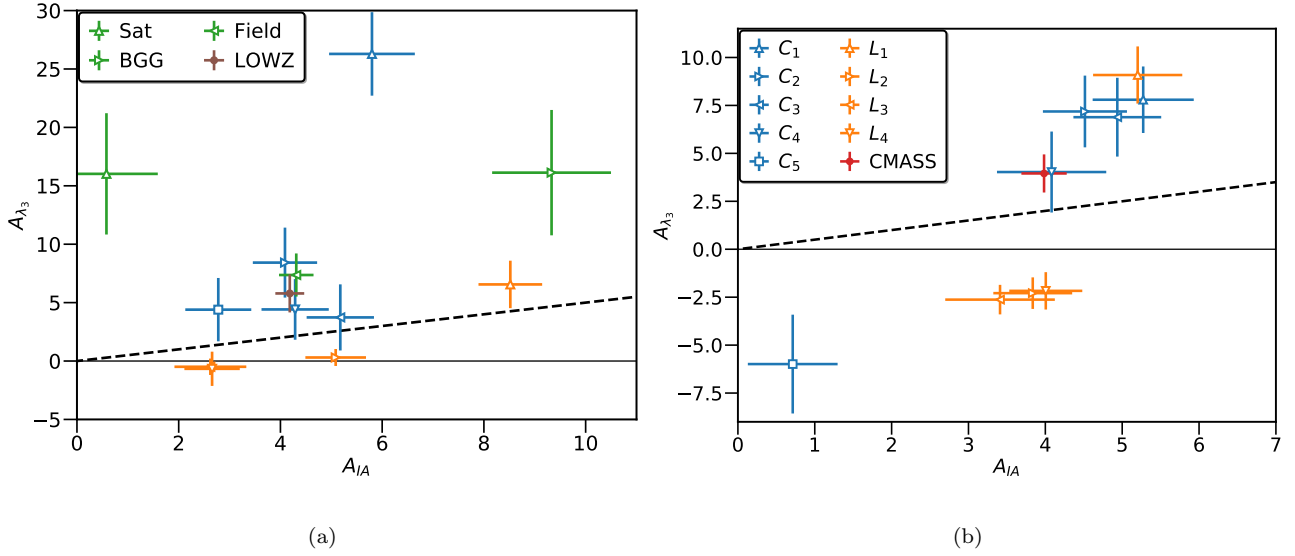


Figure 8. Comparison of the intrinsic alignments amplitude (A_{IA}) measured using galaxy shear and the amplitude of galaxy size correlations measured using the fundamental plane residuals (A_{λ_3}), for different subsamples of LOWZ (a) and CMASS (b). Different colors represent different splits and different markers represent different subsamples (labels for color and luminosity subsamples are consistent across two panels). Under the model assumed in section 2.3, size correlations are caused by intrinsic alignments in conjunction with projection effects and we expect $A_{\lambda_3} \propto A_{IA}/2$ (shown by dashed black line). Solid cyan line shows the best fit linear model with parameter as shown in the figures. Data prefers $A_{\lambda_3} \propto 4A_{IA}$, which suggests that in addition to projection effects, galaxy sizes themselves are affected by the tidal field, such that $\lambda_3 \propto \nabla^2\phi$, with similar constants as the IA model.

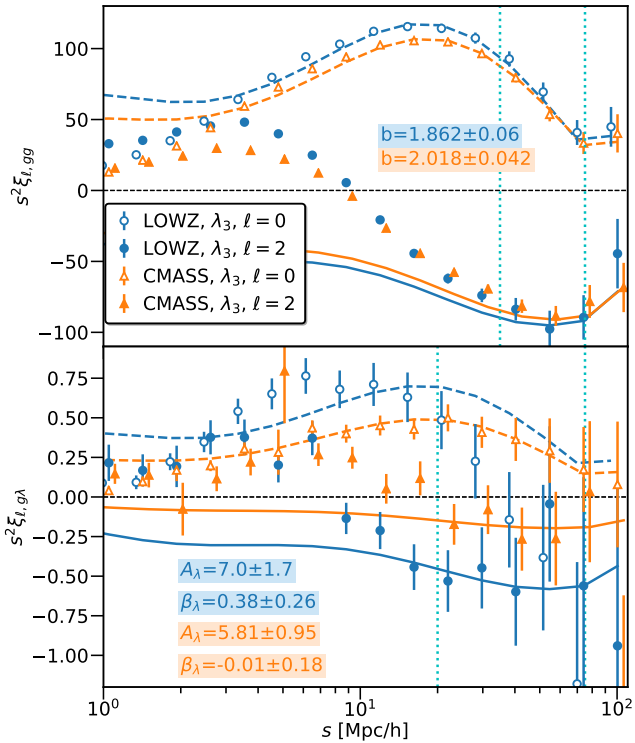


Figure 9. Measurements of the multipoles of galaxy clustering (upper panels) and galaxy- λ (lower panels) cross correlation functions for LOWZ (blue) and CMASS (orange) samples. Open points and dashed line shows the monopole and the best fit model for the monopole ($\ell = 0$) while closed points and lines show the same for quadrupole ($\ell = 2$). Vertical cyan lines mark the range over which the model was fit.

lier in Beutler et al. (2017), Grieb et al. (2016a), and Hand et al. (2017b). In our fits, we set the minimum wavenumber k_{\max} to 0.05 and $0.02 \, h\text{Mpc}^{-1}$, respectively for LOWZ and CMASS, in order to minimize any large-scale effects of the window function. As described in section 2.5, we fix the AP distortion parameters to their fiducial values and constrain 11 free parameters, of which two are primarily of our interests: the growth rate f and the amplitude of matter fluctuations σ_8 . Fitting this RSD model to the BOSS DR12 multipole measurements, we obtain a tight constraint on the growth of structure, and more detail can be found in Yu et al. (prep).

4.3.1 Fundamental plane cuts

In this section we fit FP to the LOWZ and CMASS samples, for NGC and SGC regions separately, and then split each galaxy sample into two subsamples according to the sign of the FP residuals, with the mean FP residual subtracted from each sample, following Martens et al. (2018). Samples with positive (negative) FP residuals correspond to galaxies larger (smaller) than the FP-predicted size. We then fit the galaxy power spectrum model to each of the two subsamples, constraining 11 free parameters in the RSD model presented in section 2.5.

In the analysis, we consider different types of FP residuals: FP fit with $N_z = 1$ (λ_1), FP fit with $N_z = 1$ in narrow redshift bins ($\lambda_{1,zb}$), FP fit only dependent on the surface brightness with the velocity dispersion measurements ignored (λ_1^I ; still with $N_z = 1$), FP fit equivalent to the one in Martens et al. (2018) (λ_1^M), FP fit with $N_z = 3$ (λ_3). Figure 11 shows how the model fits to each of the two subsamples of the LOWZ NGC galaxies. The subsample with positive FP residuals (henceforth called the “posi-

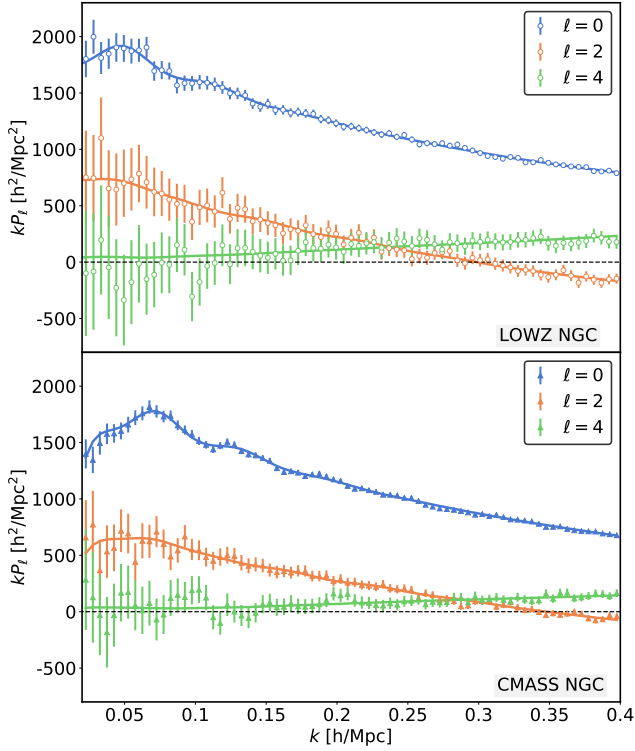


Figure 10. The measured galaxy power spectrum multipoles in Fourier space (data points) and the best-fit theory curves (solid lines) for LOWZ NGC (upper panel) and CMASS NGC (lower panel) samples. We fit the model to the monopole (blue), quadrupole (orange), and hexadecapole (green), over the wavenumber range $k = 0.05 - 0.4$ and $0.02 - 0.4 h\text{Mpc}^{-1}$ for LOWZ and CMASS galaxies, respectively. Multipoles are accurately modelled, down to $k = 0.4 h\text{Mpc}^{-1}$. Although not shown in the figure, we also find an excellent model fit to the SGC samples.

tive” subsample) has higher galaxy bias than the subsample with negative FP residuals, in agreement with the results in [Martens et al. \(2018\)](#). We also find that disregarding the velocity dispersion in the FP definition causes a larger deviation in the galaxy bias between subsamples. Some deviation in the galaxy bias is expected from the correlations between the FP and the galaxy properties as discussed in section 4.1. Since the “positive” sample preferentially selects brighter galaxies, it is expected to have larger bias.

The monopole $P_0(k)$ and the quadrupole $P_2(k)$ scale as $(b_1\sigma_8)^2$ and $b_1f\sigma_8^2$, respectively. Hence, we can roughly estimate the ratio of $f\sigma_8$ and $b_1\sigma_8$ values between two subsamples of the FP fit from the ratios of the monopoles and quadrupoles. The square rooted ratio of the monopoles scales as $b_1\sigma_8$; for the LOWZ NGC sample, the subsample with positive λ_1^I has this ratio $\approx 10\%$ larger than the subsample with negative λ_1^I . Adding the velocity dispersion term to the FP definition reduces such deviation to $\approx 6\%$. We can also take the quadrupole ratio between two samples and divide it by the square rooted ratio of their monopoles to remove the bias dependence. This quantity roughly determines the ratio of $f\sigma_8$ values between two samples. Figure 12 plots the ratios 1) between the full LOWZ NGC sample and the subsample with positive FP residuals (blue) and 2) between the full LOWZ NGC sample and the subsample with

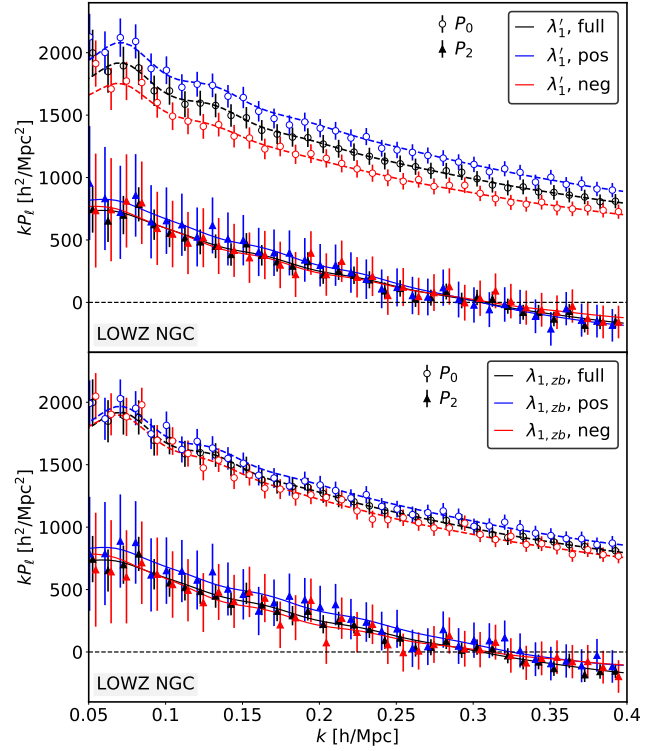


Figure 11. Multipole measurements of the LOWZ NGC subsamples with positive (blue) and negative (red) FP residuals, with different types of FP fits. Multipoles of the full LOWZ NGC sample (black) are also provided as a reference, and open circular points and closed triangular points display the monopoles and quadrupoles, respectively. We show the measured multipoles (data points) and the best-fit theory curves (solid lines) for positive and negative subsamples with two different FP definitions: FP fit without velocity dispersion (λ_1^I ; upper panel) and FP fit in narrow redshift bins ($\lambda_{1,zb}$; lower panel). The RSD model fits well to all subsamples, and other subsamples with different FP definitions similarly have good model fits, although not shown in the figure. The monopoles of positive and negative subsamples clearly have different amplitudes, suggesting the difference in their galaxy biases.

negative FP residuals (red). The measured ratios are well within 1σ from each other, particularly on the scales where non-linear, small effects are not important, suggesting that measurements of the difference in RSD constraints between the FP fit subsamples are not statistically significant.

RSD model fits in figure 13 are in agreement with the above observation. For each galaxy sample, we fit the RSD model to the multipoles of positive and negative (FP fit) subsamples, for both NGC and SGC regions, and then measure the difference in $f\sigma_8$ and $b_1\sigma_8$ constraints between two subsamples. With the convention that the value of the negative subsample is subtracted from the value of the positive subsample, we consider different types of the FP residuals (λ_1^I , λ_1 , $\lambda_{1,zb}$, λ_3 , and λ_1^M). In figure 13, FP fit subsamples selected in the same redshift range and sky region are marked in the same color, and such samples are not independent, all correlated with one another. First, we find that all positive subsamples have larger galaxy biases than negative subsamples, as expected from figure 11, thereby resulting in the sign of $\Delta b_1\sigma_8$ positive in all FP fits. On the contrary,

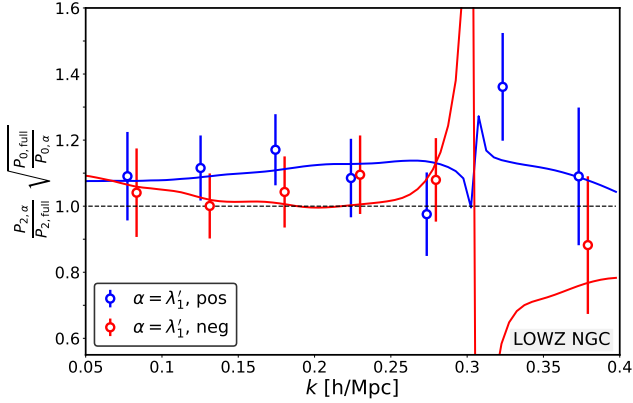


Figure 12. A rough estimate of the ratio of $f\sigma_8$ values between the full LOWZ NGC sample and FP fit subsamples, as quantified by the quadrupole ratio $(P_{2,\alpha})/(P_{2,\text{full}})$ divided by $\sqrt{(P_{0,\alpha})/(P_{0,\text{full}})}$, where α denotes the FP fit subsample. Open circular points show the measured ratios, while the dotted lines show the ratios from the best-fit theory curves. The difference in the measured ratios of the two subsamples is not statistically significant, especially on the scales where non-linear, small effects are not important.

the signs of $\Delta f\sigma_8$ measurements are not consistent across all samples and all within 1σ of the measurements, statistically consistent with the null result. This suggests that there is no evidence of significant bias in RSD measurements due to IA, in tension with the results from Martens et al. (2018), which showed a consistent offset in Δf between the FP fit subsamples. In section 2.5.1, the model expects that $\Delta b_g + \frac{1}{3}\Delta f \approx 0$, where b_g and f are galaxy bias and growth rate parameters, respectively. However, as shown in figure 13, the null model ($\Delta f \sim 0$) is favored over such theory prediction by the data points. Similarly, figure 16 and 18 in Martens et al. (2018) also show a deviation between the model and measured data points.

Martens et al. (2018) quantifies how well the measurements agree with the theoretical predictions in the following way,

$$\frac{\text{Observed}}{\text{Theory}} = \frac{\sum_i \left[\frac{B_i^{\text{Theory}}}{\sigma_i} \right]^2 \frac{B_i^{\text{Observed}}}{B_i^{\text{Theory}}}}{\sum_i \left[\frac{B_i^{\text{Theory}}}{\sigma_i} \right]^2} \pm \frac{1}{\sqrt{\sum_i \left[\frac{B_i^{\text{Theory}}}{\sigma_i} \right]^2}}, \quad (47)$$

where B_i is the parameter measuring the amplitude of intrinsic alignments for each galaxy sample i , and σ_i is the error on the measured B . Martens et al. (2018) measures Obs/Theory = 0.61 ± 0.26 . Assuming the model in Martens et al. (2018), we repeat the analysis and obtain Obs/Theory = 0.05 ± 0.30 , consistent with zero.

In figure 13, we use the MultiDark-Patchy mock catalogues to estimate the size of the error bars of RSD constraints for the FP fit subsamples. In this work, we consider four different galaxy samples: LOWZ NGC, LOWZ SGC, CMASS NGC, and CMASS SGC. For each sample, we take 100 PATCHY mocks and separate each mock into two subsamples, depending on their stellar masses, as the stellar mass is correlated with the luminosity, which in turn is correlated with the FP residuals and also correlated with the galaxy alignment strength (Joachimi et al. 2011; Singh et al.

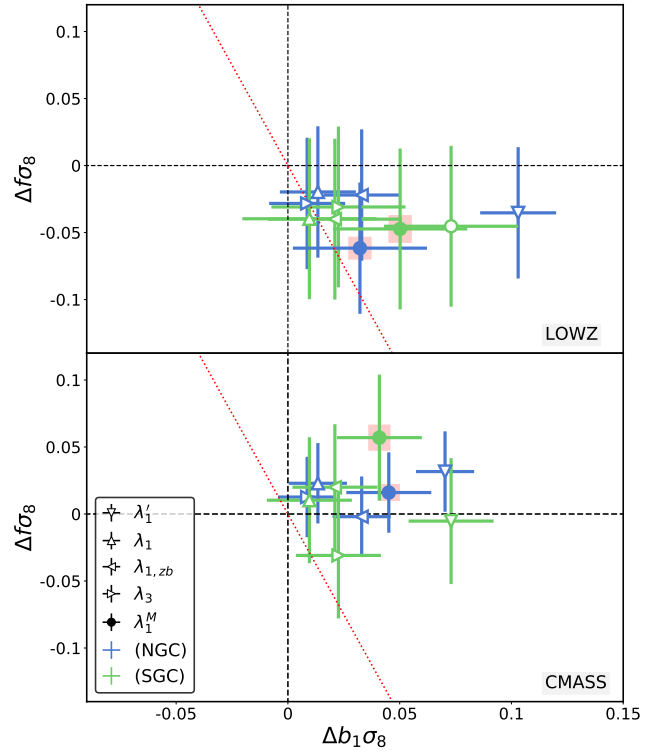


Figure 13. The measured difference in $f\sigma_8$ and $b_1\sigma_8$ between positive and negative subsamples, with different definitions of FP fits (indicated with different markers), for the LOWZ (upper panel) and CMASS (lower panel) galaxies in NGC (blue) and SGC (green) regions. Data points highlighted with red rectangles are using the FP measurements from Martens et al. (2018). Note that samples in the same color are all correlated with one another; we take the same galaxy sample and split them into the FP fit subsamples based on different FP definitions. The differences in $f\sigma_8$ values are all statistically consistent with the null results, while the signs of $\Delta b_1\sigma_8$ is consistently positive. For both LOWZ and CMASS, the theory prediction (red dotted lines) from section 2.5.1, $\Delta f \approx -3\Delta b_1$, is not favored by the data points relative to the null model ($\Delta f \sim 0$).

2015)). Consequently, we have 100 subsamples with their stellar masses larger than the mean stellar mass of the sample and 100 subsamples with their stellar masses smaller than the mean. For each galaxy sample, we then perform fits to the measured multipoles of PATCHY mocks, and the best-fitting parameters for each of the 200 subsamples are obtained by maximum a posteriori (MAP) estimation using the LBFGS algorithm. Subsequently, we measure the standard deviation of the best-fitting values of $f\sigma_8$ and $b_1\sigma_8$ and obtain the propagated error for $\Delta f\sigma_8$ and $\Delta b_1\sigma_8$. In appendix F2, we also show the statistical error obtained by random splits; however, the sample variance and noise are generally treated better with the mock results, especially given the way samples are split.

4.3.2 Luminosity/color cuts

In fig 14, with luminosity cuts as described in section 3, we divide the LOWZ NGC sample into four subsamples, with L_1 being brightest and L_4 being faintest, and show how the RSD model fits the galaxy power spectrum multipoles

of all subsamples. The measurements shown in the upper panel generally agrees with the results in appendix C: as there is a decreasing trend of bias with luminosity. Similarly the lower panel plots the quadrupole measurements of all subsamples. The measured multipoles and the best-fit theory model of other samples, such as LOWZ SGC, CMASS NGC, and CMASS SGC, show a similar trend and therefore not shown in the figure.

Fig 15 presents the monopole and quadrupole measurements of the LOWZ NGC subsamples based on the color cut, with colors going redder from C_5 to C_1 . As in figure C2, a redder subsample is shown to have a higher bias. However, the quadrupole measurement of C_1 clearly deviates from those of other subsamples, and fitting the RSD model to all color subsamples, we find that its $f\sigma_8$ constraint is significantly different from $f\sigma_8$ measurements of other subsamples. More detailed analysis can be found in appendix E.

In figure 17, we show the correlations between the constraints on $f\sigma_8(z_{\text{eff}})$, the product of f and σ_8 , each evaluated at the effective redshift of each sample, and the rescaled FP residual amplitude A_{λ_3} , computed at the fiducial σ_8 . We divide each $f\sigma_8(z_{\text{eff}})$ measurement with the predictions from the Planck 2015 data, to present $f\sigma_8$ measurements independent of the effective redshifts of our samples. To make direct comparisons with the model in section 2.5.1, we rescale A_{λ_3} and then multiply it with a factor γ/f_{fid} , where γ is the response parameter as described in section 2.5.1. The measured γ values (assuming λ_3^{NS} , where ‘NS’ denotes fitting NGC and SGC separately.) are shown in figure 16. ²

As shown in figure 17, we also find that there is only a weak evolution of the growth rate measurements with the FP residual amplitude. This agrees with the conclusion in section 4.3.1 that no significant bias in RSD measurements due to IA is evident. We quantify this correlations by fitting a linear relation between the growth rate f and the FP residual amplitude, and the following are the best-fit models: $(f\sigma_8/f\sigma_{8,\text{fid}}) = (-0.05 \pm 0.02) - (-0.36 \pm 0.14) \cdot [-\gamma A_{\lambda_3} \zeta / f_{\text{fid}}]$ for NGC and $(f\sigma_8/f\sigma_{8,\text{fid}}) = (-0.07 \pm 0.03) + (-0.10 \pm 0.04) \cdot [-\gamma A_{\lambda_3} \zeta / f_{\text{fid}}]$ for SGC, clearly in tension with the model in section 2.5.1, which predicted that the growth rate f is larger for a larger FP amplitude; we find such correlations in the opposite direction for both NGC (left panel) and SGC (right panel) samples. Moreover, the slope of this fit is largely driven by the LOWZ C_1 outlier. Without the LOWZ C_1 sample, the slope would be closer to zero. Comparing the measurements to the null detection of IA effects on RSD measurements (shown by brown lines), we obtain χ^2 values of 27.6 and 14.6 for 18 NGC and 18 SGC sub-samples, respectively. For the NGC samples, this corresponds to probability-to-exceed (PTE) of $\approx 7\%$, which indicates that the measurements are consistent with the null result.

5 CONCLUSIONS

In this work we have presented the estimations of the FP of the BOSS galaxies and the dependence of FP residuals on

² Assuming the FP definition in Martens et al. (2018), we get $\gamma = -0.21 \pm 0.03, 0.11 \pm 0.04, 0.18 \pm 0.02, 0.22 \pm 0.04$ for LOWZ NGC, LOWZ SGC, CMASS NGC, and CMASS SGC respectively.

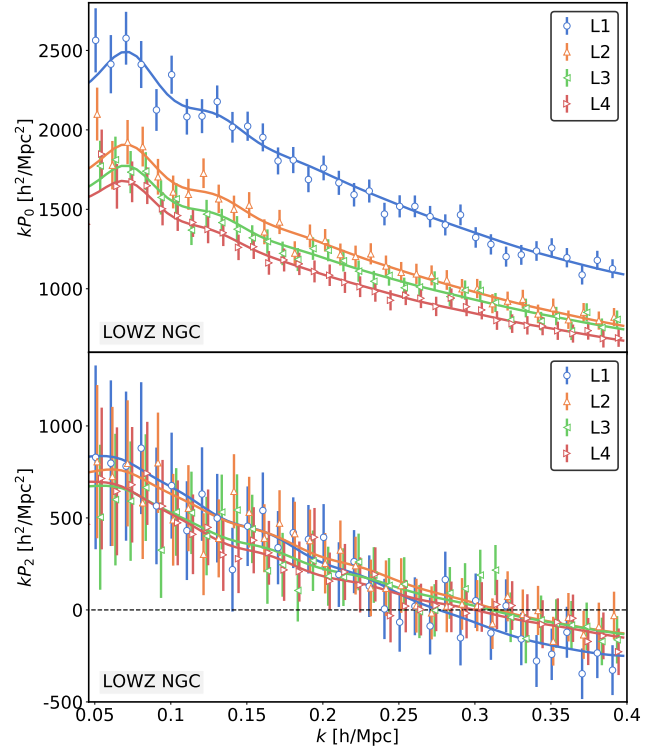


Figure 14. The measured galaxy power spectrum multipoles (data points) of four luminosity subsamples (as in figure C1), for the LOWZ NGC sample. Solid lines indicate the best-fit theory curves. The monopole measurements (upper panel) show a decreasing trend of bias with luminosity; this suggests that a brighter subsample has a higher galaxy bias. The quadrupole measurements (lower panel) of all luminosity subsamples are within 1 sigma of the quadrupole of the full sample.

the galaxy redshift, environment and luminosity. We show that the redshift evolution of the FP observed in earlier works (Joachimi et al. 2015; Saulder et al. 2019) is primarily driven by the redshift evolution of the surface brightness of the galaxies and correcting for this redshift implies that the FP is primarily a relation between the size, luminosity and velocity dispersion of the galaxies. The FP residuals are also strongly correlated with the luminosity of the galaxies and the luminosity evolution of the FP is primarily responsible for the apparent environment dependence of the FP residuals as was first detected by Joachimi et al. (2015). In appendix D we also show that the FP residuals are correlated with the observational systematics, most notably the goodness of the galaxy profile fits, the PSF flux and in the case of CMASS sample the stellar density weights.

In section 4.2 we presented the measurements and analysis of the correlations between the FP residuals and the galaxy density field, $w_{g\lambda}$. FP residuals for BOSS Lowz and CMASS samples show similar correlations with the density field. We showed that these correlations are driven by the correlations between the galaxy properties and the galaxy density field. Galaxy luminosity, size and velocity dispersion are positively correlated with the density field while the surface brightness is negatively correlated. The negative correlation of surface brightness is a non-trivial result and is potentially important for HOD modeling, relating galax-

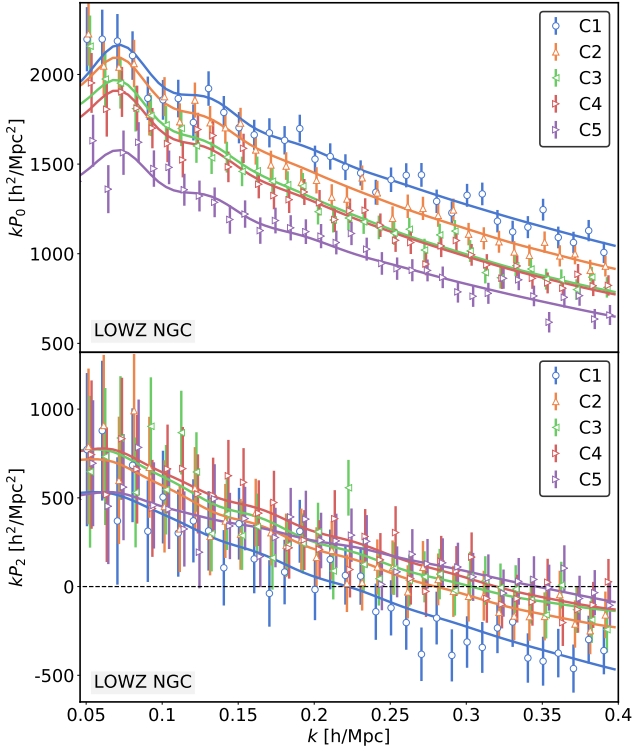


Figure 15. Similar to figure 14. The multipoles of five color subsamples (as in figure C2) for LOWZ NGC and the best-fit theory model (solid lines). The monopole measurements (upper panel) show that a redder subsample has a higher bias.

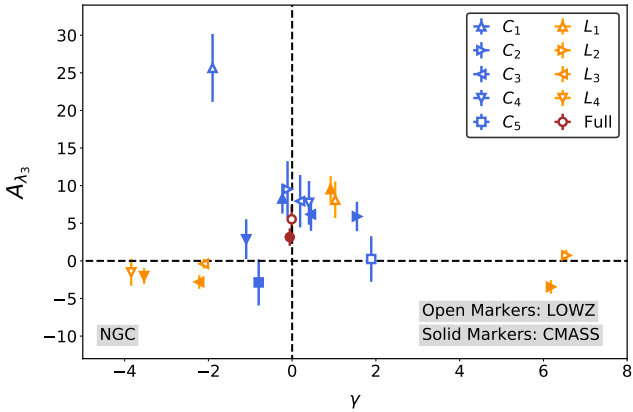


Figure 16. Comparison of the FP residuals A_{λ_3} and the selection dependence factor γ for different subsamples of LOWZ NGC and CMASS NGC. Different colors represent different splits, and different markers represent different subsamples. No correlation between A_{λ_3} and γ is evident in the figure.

ies to the halos as well for the modeling of galaxy bias as function of redshift.

We also studied the dependence of the $w_{g\lambda}$ as function of galaxy environment, luminosity as well as color. Brighter galaxies show strong positive correlations between the FP residuals and the density field while the correlation amplitude is lower for fainter samples with the lowest luminosity sample showing negative correlations. Similar trends are also observed for the color splits, with strong positive corre-

lations for the red galaxies with lower correlations for bluer samples. Combining all the samples together, we show that there is strong correlation between the galaxy bias and the amplitude of $w_{g\lambda}$. This implies that the galaxies in more over dense regions show stronger correlations between the FP/size residuals and the environment.

We also compare the amplitude of $w_{g\lambda}$ measurements from model fits with amplitude of the intrinsic alignment (IA) measurements. Since our model assumes that the size correlations are sourced by the effects of IA in three dimensions projected onto the two dimensional plane of the sky, the amplitudes of IA and $w_{g\lambda}$ measurements are expected to be the same. Though there is considerable scatter, our results are in tension with this prediction. We further tested the model by measuring the multipole moments of the correlation functions, finding again that the measured multipole moments are in tension with the model predictions. We note that our modeling has a limitation as we do not include the density weighting effects. Thus while measurements are in tension with the incomplete model, it is difficult to conclude that the IA does not have any impact on the size correlations as estimated using the FP.

Furthermore, in section 4.3 we presented the correlations between FP residuals and RSD constraints, in particular on the growth rate parameter. Splitting the BOSS LOWZ and CMASS galaxies into subsamples based on FP residuals, we fitted the RSD model to the measured multipoles of each subsample and showed that the differences in RSD constraints, across all subsamples, are statistically consistent with the null result. We hence conclude that there is no evidence of significant impact in RSD measurements due to IA, contrary to conclusions drawn by Martens et al. (2018). Moreover, the RSD measurements of the BOSS samples split by luminosity and color further strengthens this argument; despite some scatter, we find only a weak evolution of the RSD constraints with the FP residual amplitude, and in comparison with the model from Martens et al. (2018), we find this effect in the opposite direction. This suggest that there can be other overwhelming effects that impact the FP, and it can be difficult to simply disentangle the relation among FP, IA, and RSD measurements from other effects.

Our work is a step towards improved understanding of FP to use it as a tool for studying galaxies as well as cosmology. The scatter in the FP is similar to the scatter in the ellipticities of the galaxies, suggesting that it can be developed as a probe of gravitational lensing and beyond with similar potency as the galaxy ellipticities (shear). There are notable impediments to such applications as the FP is dependent on the galaxy properties, environment, selection effects and photometry errors. A deeper understanding of the impact of galaxy physics on the FP will require a similar study as ours using realistic cosmological simulations that we plan to pursue in near future. A detailed understanding of observational effects will require image simulations as were performed for the context of galaxy shape measurements (e.g. Mandelbaum et al. 2018). A more detailed modeling for the FP correlations with density field also needs to be developed to capture the information from small scales that we ignored in this work as well as to capture the impact of density weighting terms. The promise of galaxy sizes for cosmological applications and the upcoming large dataset from

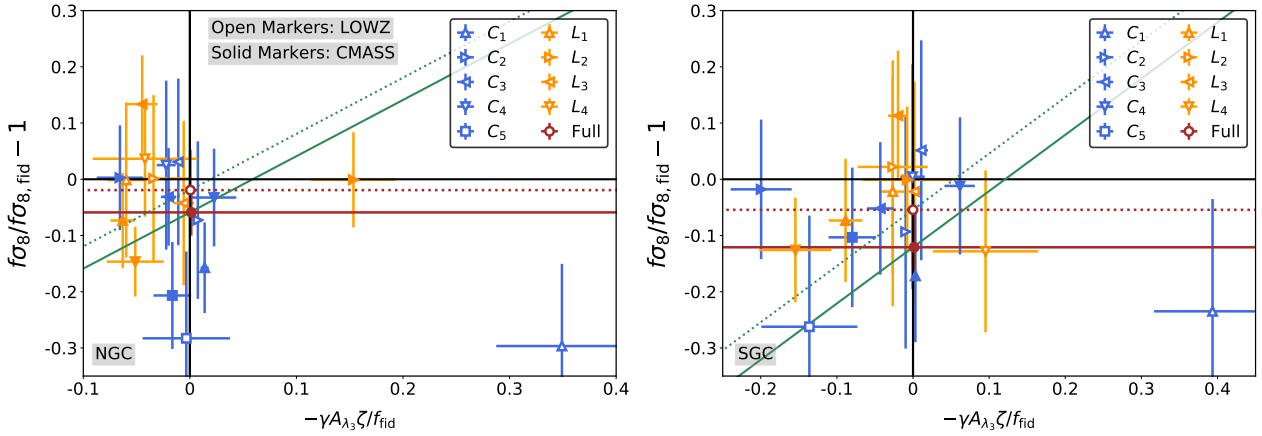


Figure 17. Comparison of the RSD measurements of the growth of structure and the rescaled FP residual amplitude, for different subsamples of LOWZ (open markers) and CMASS (solid markers) galaxies in NGC (left panel) and SGC (right panel) regions. Each measurement of $f\sigma_8(z_{\text{eff}})$ is divided by the predicted value assuming the fiducial Planck 2015 cosmology (y -axis), and the amplitude of galaxy size correlations measured using the FP residuals (A_{λ_3}) is rescaled and multiplied by $-\gamma\zeta/f_{\text{fid}}(z_{\text{eff}})$ of each sample (x -axis) so that the expected correlation coefficient between two variables is 1, according to $\Delta f = -\gamma A_{\lambda_3} \zeta$ (eq. 42). Green lines represent the expected relation between the FP residual and RSD measurements for the full LOWZ (dotted lines) and CMASS (solid lines) sample, and similarly brown lines show the growth of structure measurements for the full LOWZ and CMASS samples. We find that there is only a weak evolution of the growth of structure measurements with the FP residual amplitude, thereby suggesting that no significant bias in RSD measurements due to IA is evident.

DESI, LSST, Euclid and WFIRST makes it an opportune moment to study FP and galaxy sizes in general in more detail.

ACKNOWLEDGMENTS

We thank Rachel Mandelbaum, Chris Hirata, Alexie Leauthaud and Song Huang for useful discussions related to this work. We also thank Chris Hirata for providing access to data from [Martens et al. \(2018\)](#) and Rachel Mandelbaum for providing access to the galaxy shape measurements used for IA measurements. This material is based upon work supported by the National Science Foundation under Grant Numbers 1814370 and NSF 1839217, and by NASA under Grant Number 80NSSC18K1274.

REFERENCES

Abazajian K. N., et al., 2009, *ApJS*, **182**, 543
Ahn C. P., et al., 2012, *ApJS*, **203**, 21
Aihara H., et al., 2011, *ApJS*, **193**, 29
Alam S., et al., 2015, *ApJS*, **219**, 12
Baldauf T., Smith R. E., Seljak U., Mandelbaum R., 2010, *Phys.Rev.D*, **81**, 063531
Bernardi M., et al., 2003, *The Astronomical Journal*, **125**, 1866
Bertin G., Lombardi M., 2006, *ApJ*, **648**, L17
Beutler F., et al., 2017, *Mon. Not. Roy. Astron. Soc.*, **466**, 2242
Bianchi D., Gil-Marín H., Ruggeri R., Percival W. J., 2015, *Mon. Not. Roy. Astron. Soc.*, **453**, L11
Blanton M. R., Lin H., Lupton R. H., Maley F. M., Young N., Zehavi I., Loveday J., 2003, *AJ*, **125**, 2276
Blazek J., McQuinn M., Seljak U., 2011, *J. Cosmology Astropart. Phys.*, **5**, 10
Blazek J., Vlah Z., Seljak U., 2015, *J. Cosmology Astropart. Phys.*, **2015**, 015
Bolton A. S., et al., 2012, *AJ*, **144**, 144

Bonvin C., Andrianomena S., Bacon D., Clarkson C., Maartens R., Moloi T., Bull P., 2017, *Monthly Notices of the Royal Astronomical Society*, **472**, 3936
Dawson K. S., et al., 2013, *AJ*, **145**, 10
Djorgovski S., Davis M., 1987, *The Astrophysical Journal*, **313**, 59
Dressler A., Lynden-Bell D., Burstein D., Davies R. L., Faber S. M., Terlevich R., Wegner G., 1987, *The Astrophysical Journal*, **313**, 42
Eisenstein D. J., et al., 2001, *AJ*, **122**, 2267
Fukugita M., Ichikawa T., Gunn J. E., Doi M., Shimasaku K., Schneider D. P., 1996, *AJ*, **111**, 1748
Grieb J. N., et al., 2016a, preprint, ([arXiv:1607.03143](#))
Grieb J. N., Sanchez A. G., Salazar-Albornoz S., Dalla Vecchia C., 2016b, *Mon. Not. Roy. Astron. Soc.*, **457**, 1577
Gunn J. E., et al., 1998, *AJ*, **116**, 3040
Gunn J. E., et al., 2006, *AJ*, **131**, 2332
Hand N., Li Y., Slepian Z., Seljak U., 2017a, *JCAP*, **1707**, 002
Hand N., Seljak U., Beutler F., Vlah Z., 2017b, *JCAP*, **1710**, 009
Hand N., Feng Y., Beutler F., Li Y., Modi C., Seljak U., Slepian Z., 2018, *Astron. J.*, **156**, 160
Hartlap J., Simon P., Schneider P., 2007, *A&A*, **464**, 399
Hirata C. M., 2009, *MNRAS*, **399**, 1074
Hirata C., Seljak U., 2003, *MNRAS*, **343**, 459
Hogg D. W., Finkbeiner D. P., Schlegel D. J., Gunn J. E., 2001, *AJ*, **122**, 2129
Huff E. M., Graves G. J., 2011, arXiv e-prints, p. [arXiv:1111.1070](#)
Ivezić Ž., et al., 2004, *Astronomische Nachrichten*, **325**, 583
Joachimi B., Mandelbaum R., Abdalla F. B., Bridle S. L., 2011, *A&A*, **527**, A26
Joachimi B., Singh S., Mandelbaum R., 2015, *MNRAS*, **454**, 478
Kaiser N., Squires G., Broadhurst T., 1995, *ApJ*, **449**, 460
Landy S. D., Szalay A. S., 1993, *ApJ*, **412**, 64
Lesgourgues J., 2011, preprint, ([arXiv:1104.2932](#))
Li Y., Singh S., Yu B., Feng Y., Seljak U., 2019, *J. Cosmology Astropart. Phys.*, **2019**, 016
Lupton R., Gunn J. E., Ivezić Z., Knapp G. R., Kent S., 2001, in Harnden Jr. F. R., Primini F. A., Payne H. E., eds, *Astronomical Society of the Pacific Conference Series Vol. 238, Astronomical Data Analysis Software and Systems X*. p. 269

- ([arXiv:astro-ph/0101420](#))
Mandelbaum R., et al., 2011, *MNRAS*, **410**, 844
Mandelbaum R., et al., 2018, *MNRAS*, **481**, 3170
Martens D., Hirata C. M., Ross A. J., Fang X., 2018, *MNRAS*, **478**, 711
Nigoche-Netro A., Ruelas-Mayorga A., Franco-Balderas A., 2009, *MNRAS*, **392**, 1060
Okumura T., Seljak U., McDonald P., Desjacques V., 2012a, *J. Cosmology Astropart. Phys.*, **2012**, 010
Okumura T., Seljak U., Desjacques V., 2012b, *J. Cosmology Astropart. Phys.*, **2012**, 014
Okumura T., Hand N., Seljak U., Vlah Z., Desjacques V., 2015, *Phys. Rev.*, **D92**, 103516
Padmanabhan N., et al., 2008, *ApJ*, **674**, 1217
Pier J. R., Munn J. A., Hindsley R. B., Hennessy G. S., Kent S. M., Lupton R. H., Ivezić Ž., 2003, *AJ*, **125**, 1559
Planck Collaboration et al., 2015, preprint, ([arXiv:1502.01589](#))
Reid B. A., Spergel D. N., 2009, *ApJ*, **698**, 143
Reyes R., Mandelbaum R., Gunn J. E., Nakajima R., Seljak U., Hirata C. M., 2012, *MNRAS*, **425**, 2610
Richards G. T., et al., 2002, *AJ*, **123**, 2945
Ross A. J., et al., 2012, *MNRAS*, **424**, 564
Saulder C., Mieske S., Zeilinger W. W., Chilingarian I., 2013, *A&A*, **557**, A21
Saulder C., Steer I., Snaith O., Park C., 2019, arXiv e-prints, [p. arXiv:1905.12970](#)
Scoccimarro R., 2015, *Phys. Rev.*, **D92**, 083532
Scodeggio M., Gavazzi G., Belsole E., Pierini D., Boselli A., 1998, *MNRAS*, **301**, 1001
Seljak U., McDonald P., 2011, *JCAP*, **1111**, 039
Seljak U., Yu B., 2019
Singh S., Mandelbaum R., 2016, *MNRAS*, **457**, 2301
Singh S., Mandelbaum R., More S., 2015, *MNRAS*, **450**, 2195
Singh S., Mandelbaum R., Seljak U., Slosar A., Vazquez Gonzalez J., 2017, *MNRAS*, **471**, 3827
Smee S. A., et al., 2013, *AJ*, **146**, 32
Smith J. A., et al., 2002, *AJ*, **123**, 2121
Strauss M. A., Willick J. A., 1995, *Phys.Rep.*, **261**, 271
Strauss M. A., et al., 2002, *AJ*, **124**, 1810
Takahashi R., Sato M., Nishimichi T., Taruya A., Oguri M., 2012, *ApJ*, **761**, 152
Tolman R. C., 1930, *Proceedings of the National Academy of Science*, **16**, 511
Tucker D. L., et al., 2006, *Astronomische Nachrichten*, **327**, 821
Vlah Z., Seljak U., McDonald P., Okumura T., Baldauf T., 2012, *J. Cosmology Astropart. Phys.*, **2012**, 009
Vlah Z., Seljak U., Okumura T., Desjacques V., 2013, *JCAP*, **1310**, 053
Wake D. A., et al., 2006, *MNRAS*, **372**, 537
Yamamoto K., Nakamichi M., Kamino A., Bassett B. A., Nishioka H., 2006, *Publ. Astron. Soc. Jap.*, **58**, 93
York D. G., et al., 2000, *AJ*, **120**, 1579
Yu B., Seljak U., Singh S., Li Y., Hand N., in prep.
de Carvalho R. R., Djorgovski S., 1992, *The Astrophysical Journal*, **389**, L49

APPENDIX A: COMPARISON WITH MARTENS ET AL. (2018)

A1 Notation and parameters

Martens et al. (2018) definition of size residuals, W , is related to our definition of λ as

$$W = -4\lambda \quad (\text{A1})$$

W is related to the tidal field as (following notation from

Martens et al. (2018))

$$W = 2Bs_{33} = 2 \times 1.74b_{\kappa}s_{33}, \quad (\text{A2})$$

b_{κ} is written in terms of intrinsic alignments amplitude as

$$W = -2 \times 1.74A_I\zeta s_{33} \quad (\text{A3})$$

From our model for λ , we can relate the model parameters as

$$-4A_{\lambda}\zeta s_{33} = -2 \times 1.74A_I\zeta s_{33} \quad (\text{A4})$$

$$A_{\lambda} = \frac{1.74}{2}A_I \quad (\text{A5})$$

To relate the errors in the galaxy selection functions, we note that the error for a given galaxy should not depend on the definition of the FP residuals but do depend on the sign, following which we can write

$$\epsilon(\lambda) \equiv -\epsilon(W) \Rightarrow \gamma\lambda \equiv -(\eta\chi)W \quad (\text{A6})$$

This allows us to relate γ to $(\eta\chi)$ as

$$\gamma = 4(\eta\chi) \quad (\text{A7})$$

We can also derive the $\Delta(\eta\chi)$ parameter from Martens et al. (2018), in terms of the derivative of the $S(\lambda)$ which can be written as

$$\frac{dS(\lambda)}{d\lambda} = \frac{1}{(N_{\lambda+} + N_{\lambda-})^2} \left[2N_{\lambda-} \frac{dN_{\lambda+}}{d\lambda} - 2N_{\lambda+} \frac{dN_{\lambda-}}{d\lambda} \right] \quad (\text{A8})$$

$$\approx \frac{1}{2N_{\lambda}} \left[\frac{dN_{\lambda+}}{d\lambda} - \frac{dN_{\lambda-}}{d\lambda} \right] = 2\Delta(\eta\chi) \quad (\text{A9})$$

where we wrote $N_{\lambda} \approx N_{\lambda+} \approx N_{\lambda-}$. We note that eq. (A7) and eq. (A9) are not necessarily consistent with each other and we only use them to compare the numerical quantities across the two studies.

In figure A1, we show a histogram representing the distribution of $S(\lambda)$ and $\frac{\partial S(\lambda)}{\partial \lambda}$, produced by splitting galaxies into 41 λ bins. Assuming the FP definition in Martens et al. (2018), we obtain $\frac{dS(\lambda)}{d\lambda}|_{\lambda=0} = -1.69 \pm 0.09, -1.28 \pm 0.12, -1.22 \pm 0.06, -0.87 \pm 0.07$ for LOWZ NGC, LOWZ SGC, CMASS NGC, and CMASS SGC, respectively. Similarly with $\lambda = \lambda_3$, we measure $\frac{dS(\lambda)}{d\lambda}|_{\lambda=0} = -0.97 \pm 0.09, -0.68 \pm 0.13, -1.12 \pm 0.05, -0.87 \pm 0.08$ for LOWZ NGC, LOWZ SGC, CMASS NGC, and CMASS SGC, respectively.

A2 Comparison of FP definitions

To rule out the differences due to the FP definitions, we also define the FP in terms of magnitude, M , instead of surface brightness as

$$\log R_0 = b(M + 10 \log z) + c + \sum_{i=1}^{N_z} d_i z^i \quad (\text{A10})$$

$$\lambda_{N_z}^M = \ln \frac{R_0}{R_{FP,N_z}^I} \quad (\text{A11})$$

where λ_1^M is closest to the definition of FP used by Martens et al. (2018). We note that the $\lambda_{N_z}^M$ and $\lambda_{N_z}^I$ obtained by the minimizing the scatter around the plane (minimize λ_{rms}) are not the same as the two planes get different weights and hence different contributions to scatter from the magnitude and size, $\log R$. The scatter plot between the two planes is shown in fig. A2. The λ_1^M we obtain is consistent

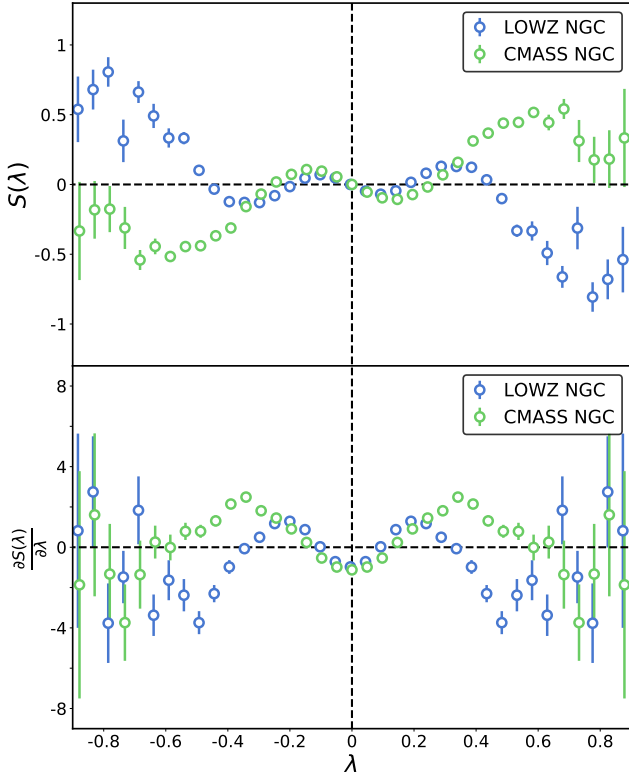


Figure A1. Histogram showing the distribution of $S(\lambda)$ (upper panel) and $\frac{\partial S(\lambda)}{\partial \lambda}$ (lower panel) values from LOWZ NGC and CMASS NGC samples. We assume $\lambda = \lambda_3$.

with the $-W_{33}/4$ from [Martens et al. \(2018\)](#), with the very small scatter which is sourced by different treatment of k-corrections and smaller differences in the cosmology across the two studies. We observe that the scatter in λ_1^M is ~ 2 times larger than the scatter in λ_1^I . We caution against interpreting λ_1^I as better using scatter as metric since scatter of the λ is simply determined by the weighted combination of the magnitude and size which are not perfectly correlated. The correlation coefficient for $\log R$ and magnitude is ~ 0.5 while for the $\log R$ and $\log I$ is ~ -0.82 .

APPENDIX B: ANALYSIS WITH i BAND

In fig. B1 we show the comparison of A_λ values obtained from the fits in the r band and the i band. For the LOWZ sample, the results between the two bands are consistent. We also tested the comparison between the de Vaucouleurs and the model magnitudes in the i band (they are same in the r band except for a very small fraction of galaxies that have exponential profiles). The two magnitudes measure also give consistent results in the i band for the LOWZ sample. For the CMASS sample on the other hand, we observe differences in the A_λ values between r band and the i band. These differences are consistent with an additive shift in A_λ . Such differences can be caused by the variations in the photometry across two bands as the 4000 angstrom line break moves into r band at $z \sim 0.4$ and hence the measurements in r band will be noisier and relatively biased with respect to i band. We also observe similar differences when using de

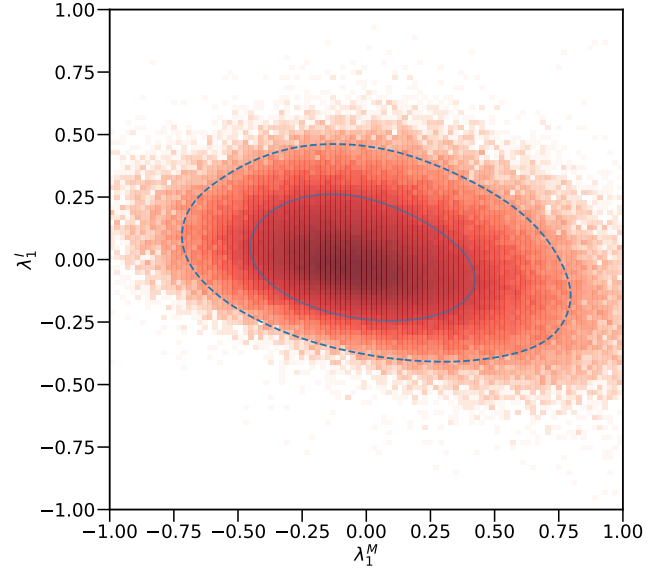


Figure A2. Comparison of the FP residuals obtained using the surface brightness in the FP, λ_1^I and the magnitudes in FP, λ_1^M . The solid and dashed blue lines show the 68% and 95% contours while the red color shows the underlying two dimensional histogram (color scaling is in log). The two FP definitions show only weak correlations and the scatter in λ_1^M is ~ 2 times larger.

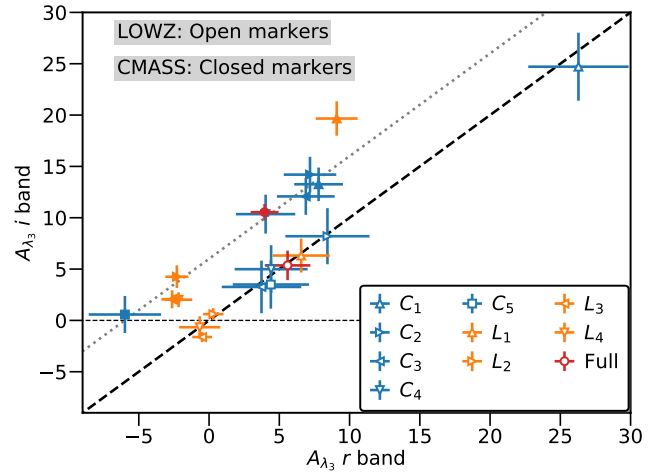


Figure B1. Comparison of A_λ constraints obtained using r band (x-axis) and i band photometry. For the LOWZ sample, both r band and i band give consistent results, while for the CMASS sample, there is an additive shift with $A_{\lambda,i} \approx A_{\lambda,r} + 6$ (shown by dotted gray line). The variation in CMASS sample is likely driven by the photometry differences due to redshift effects as 4000 angstrom line break moves into r band at $z \sim 0.4$.

Vaucouleurs and model magnitudes. For CMASS, a larger fraction of galaxies have exponential profiles and hence FP from de Vaucouleurs and model magnitudes can show larger differences leading to differences in A_λ .

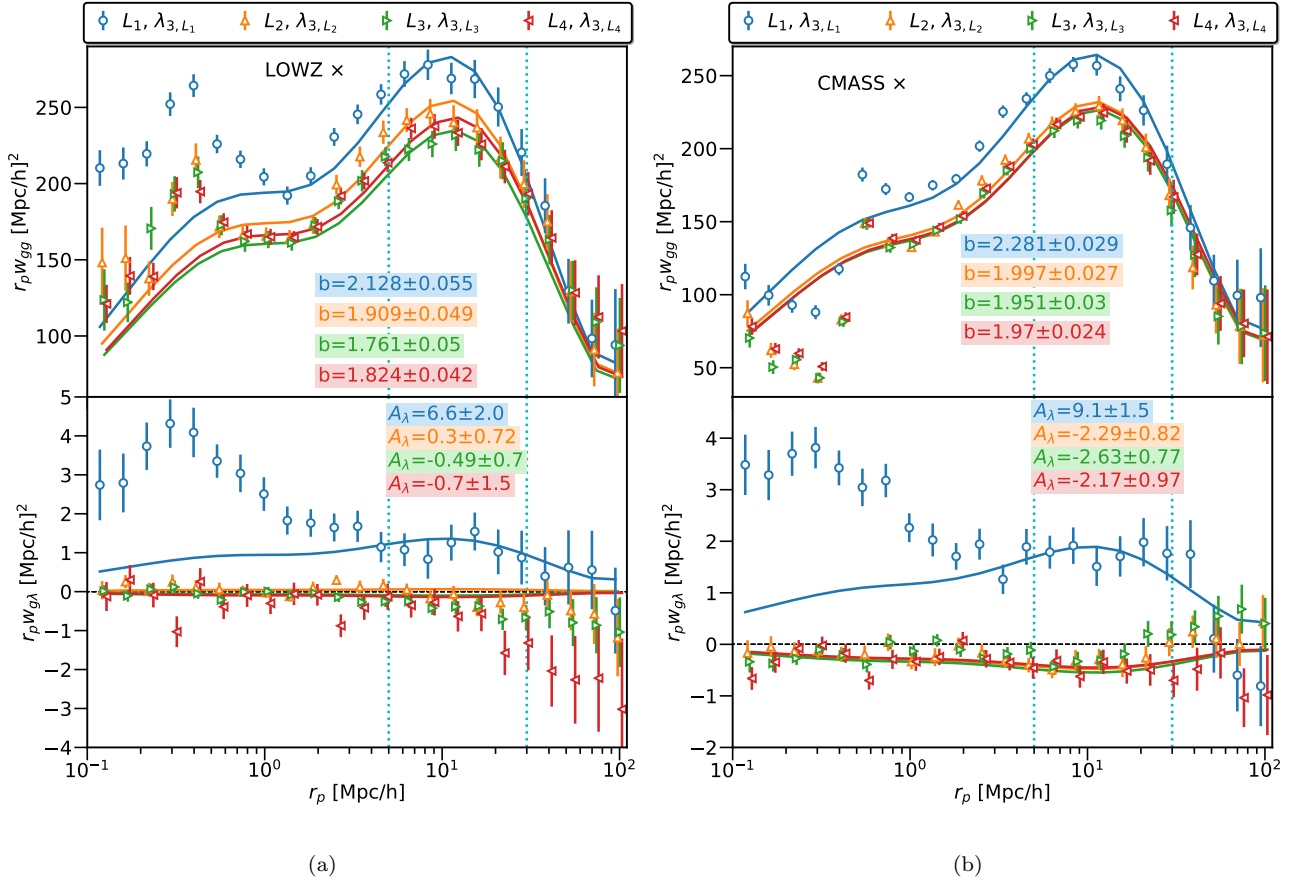


Figure C1. Galaxy clustering and galaxy- λ cross correlation functions for different luminosity sub-samples for (a) Lowz and (b) CMASS samples. For both galaxy clustering and galaxy- λ correlations, we use the full LOWZ or CMASS sample as the density tracers. Here, λ is obtained by fitting FP separately to each subsample. Luminosity samples are arranged from brightest to faintest with L_1 being brightest and L_4 being faintest. L_1 – L_3 each contain 20% of the sample and L_4 contains 40% of the sample and these samples are defined in narrow redshift bins such that the overall redshift selection, $p(z)$ is same for all samples. FP residuals for L_1 sample show significant correlations with the galaxy density while L_2 and L_3 samples are consistent with no correlations. The faintest sample L_4 shows negative correlations.

APPENDIX C: LUMINOSITY AND COLOR SAMPLES

In figure C1, we show the galaxy- λ cross correlations using subsamples based on luminosity cuts as described in section 3, with L_1 being brightest and L_4 being faintest. Note that we fit FP separately to each of these samples with the residuals labeled as λ_{3,L_i} .

From galaxy clustering, we obtain largest galaxy bias for the brightest sample, L_1 with bias decreasing with luminosity for L_2 and L_3 though L_4 sample has higher bias. The decreasing trend of bias with Luminosity is consistent with the expectations that lower luminosity galaxies tend to be in lower mass halos which have lower bias. L_4 defies this trend, likely due to relatively higher fraction of satellite galaxies within this sample, which tend to be in higher mass halos and hence have higher bias.

The brightest sample show the largest correlations with the density, implying that within the brightest sample, larger galaxies reside in over dense regions. For the fainter samples, L_2 and L_3 samples give null signal, though we note that for both of these samples rms of λ_{3,L_i} is much smaller (by a factor of ~ 2) than the rms obtained for same galaxies when

using the FP fit to the full LOWZ or CMASS samples, unlike L_1 and L_4 samples for which rms remains similar. Lower rms of λ also results in lower errors in A_λ for L_2 and L_3 samples. Furthermore, the amplitude of A_λ for these samples also show low amplitude. We confirmed that this is driven by the low amplitudes of the correlations of both size and surface brightness with the density field (plots not shown).

In figure C2, we show the galaxy- λ cross correlations using subsamples based on color cuts, with colors going from red to blue from C_1 to C_5 samples. We find that the redder samples show stronger correlations with the density though the trend is not very strong from C_3 – C_5 samples and in the CMASS galaxies. The LOWZ C_1 sample is an outlier, as it has a very large relative to other subsamples of the LOWZ galaxies. We analyze this sample further in following section, appendix C1, and show that amplitude of C_1 sample is driven by strong evolution of A_λ in the redder part of the LOWZ sample. We also split C_1 sample by redshift but do not observe any significant redshift evolution.

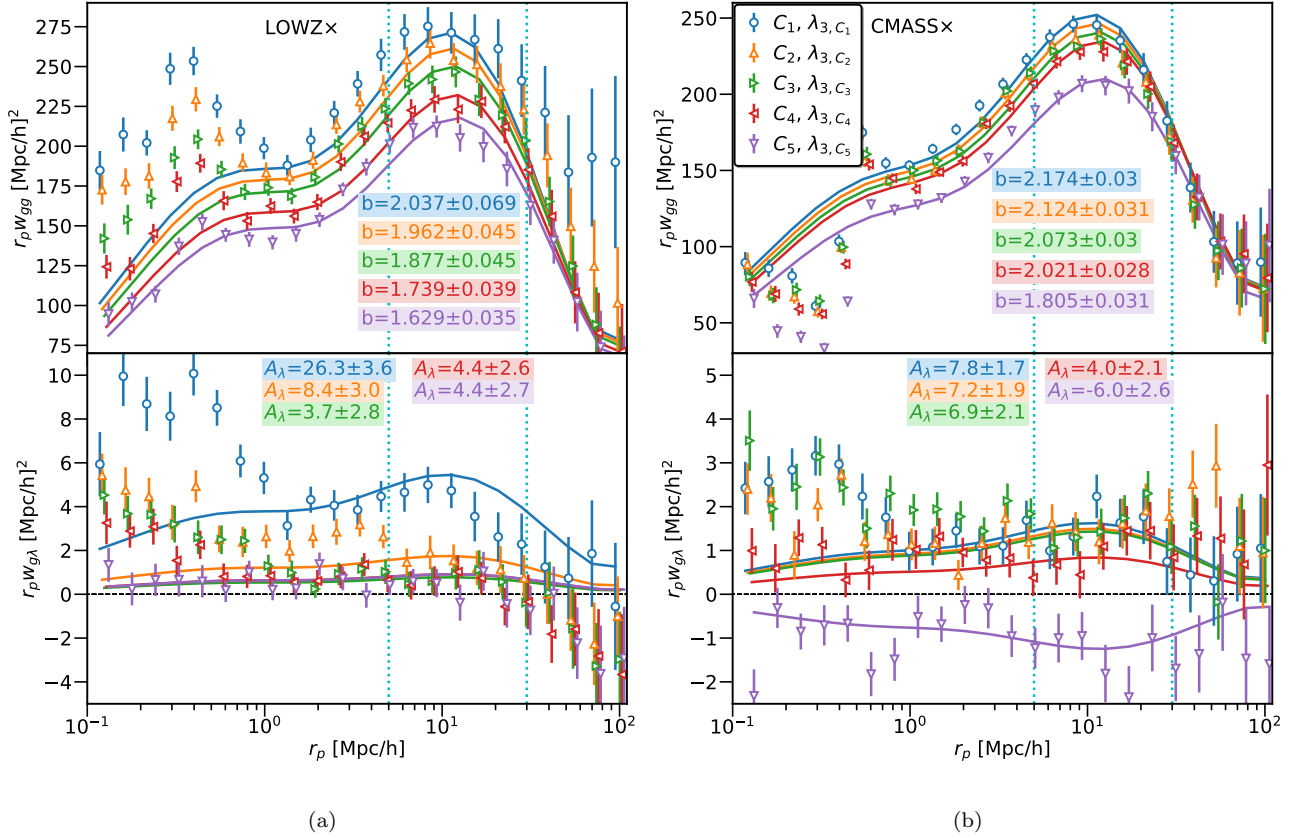


Figure C2. Similar to figure C1, the LOWZ and CMASS samples now split by color into five subsamples, with each sample containing 20% of the sample. We observe variations in the galaxy- λ correlations, with redder samples showing stronger correlations. Note that the labelling of the sub-samples is same across the two panels.

C1 Lowz C_1 sample

In this section we study the FP cross correlations of the LOWZ- C_1 subsample, which has high A_λ when compared to the other samples and the expectations from bias evolution.

In figure C3, we show the results from splitting the C_1 sample into two subsamples based on the redshift cut, with $z_1 \in [0.15, 0.3]$ and $z_2 \in [0.3, 0.43]$. We detect no redshift evolution of the results, suggesting that the C_1 constraints are robust against any redshift evolution and the high A_λ is not dominated by any small redshift slice.

Next we further split the C_1 sample into four smaller subsamples based on the color, using the same methodology as the original color splits. We denote these samples as $C_{1,i}$, where i denotes the index of the sub-subsample. In figure C4, we observe a strong trend in A_λ for the C_1 subsamples, with redder samples having larger amplitude and all of subsamples have larger amplitude than the C_2 sample. These result hint that on the redder end of the LOWZ sample, there is a strong and smooth evolution in A_λ with color and high amplitude observed for C_1 sample is a manifestation of this trend.

APPENDIX D: SYSTEMATICS TESTS

In figure D1, we show the dependence of the FP residuals on some measures of the photometric quantities or systematics, namely the log likelihood difference between the de

Vaucouleurs and exponential profile fits, PSF flux as well as stellar weights for CMASS galaxies, which depend on the stellar density on the sky. While we tested for the impact of other observational systematics, we are only showing results for the ones where we detected significant variations in $\langle \lambda_3 \rangle$, i.e. $\langle \lambda_3 \rangle$ is same order as the rms of λ_3 . Correlations in figure D1 can be understood in terms of the impact of these properties on the galaxy size and luminosity estimates as shown in the same figure.

APPENDIX E: SYSTEMATICS TESTS-II: CORRELATION FUNCTIONS

E1 Randoms re-weighting

Since the estimates of galaxy properties such as color and luminosity are affected by the observational systematics, which can vary over the sky, splitting the samples by these properties can then lead to subsamples with significantly different selection functions. While our splitting method ensures that the selection function with redshift is not affected, we do not impose any such control in the sky coordinates (RA, DEC). To lowest order, the incorrect selection function (randoms) changes the observed galaxy over-density field as

$$\hat{\delta}_g = \delta_g + \delta_{\text{sys}} \quad (\text{E1})$$

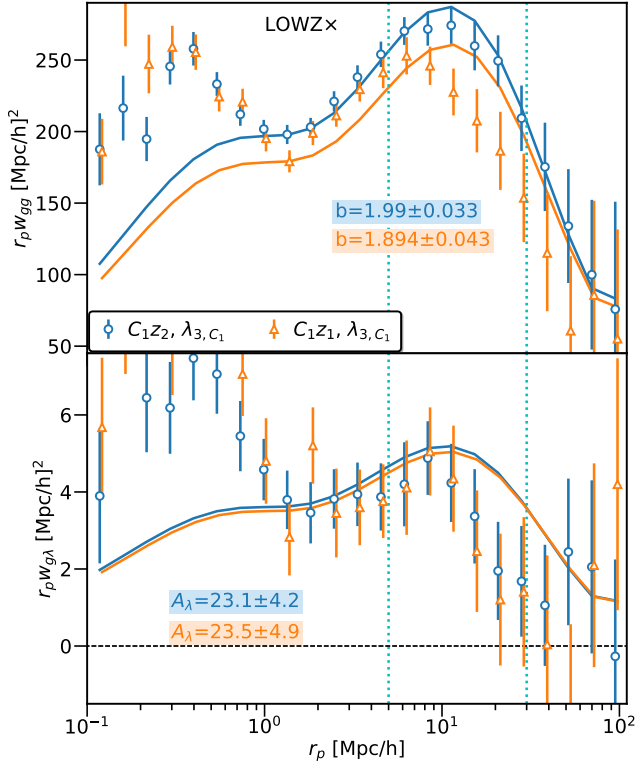


Figure C3. Splitting the Lowz C_1 sample into two subsamples based on redshift, with $z_1 \in [0.16, 0.3]$ and $z_2 \in [0.3, .43]$. Both samples give consistent results, suggesting that there is no significant evolution with redshift.

which in turn biases the correlation function and the covariance as (here we only show the equation in symbolic notation. See for example [Singh et al. \(2017\)](#) for a derivation of a similar effect)

$$\langle \hat{\delta}_g \hat{\delta}_g \rangle(\vec{r}) = \langle \delta_g \delta_g \rangle(\vec{r}) + \langle \delta_{\text{sys}} \delta_{\text{sys}} \rangle(\vec{r}) \quad (\text{E2})$$

$$\text{Cov}(\hat{\delta}_g \hat{\delta}_g, \hat{\delta}_g \hat{\delta}_g)(\vec{r}_1, \vec{r}_2) = \text{Cov}(\delta_g \delta_g, \delta_g \delta_g)(\vec{r}_1, \vec{r}_2) + \text{Cov}(\delta_{\text{sys}} \delta_{\text{sys}}, \delta_{\text{sys}} \delta_{\text{sys}})(\vec{r}_1, \vec{r}_2) \quad (\text{E3})$$

To reduce the impact of correlations from the systematics, for the subsamples we re-weight the randoms for subsamples by the ratio of number of galaxies within the subsample to the number of galaxies in the parent sample, i.e.

$$\text{Rwt}(\vec{x}) = \frac{n_{\text{subsample}}}{n_{\text{full}}}(\vec{x}, s) \quad (\text{E4})$$

where s denotes the pixelization scale of density field. For s , we try pixelization imposed by the Ipoly (pixelization scheme provided in BOSS catalogs) or the $\sim 80 \text{ deg}^2$ regions we used for the jackknife covariances.

In figure E1 we show an example demonstrating the effects of selection functions and the re-weighting of the randoms to correct for it, for the Lowz C_1 sample. Without any corrections, the correlation function measurements show large bias on the large scales. However, measurements on those scales are also very correlated (systematics impact on the covariance), and the best fit galaxy bias we obtain from this measurement is nearly unbiased (agrees with bias from cross correlations with full sample). To correct the bias

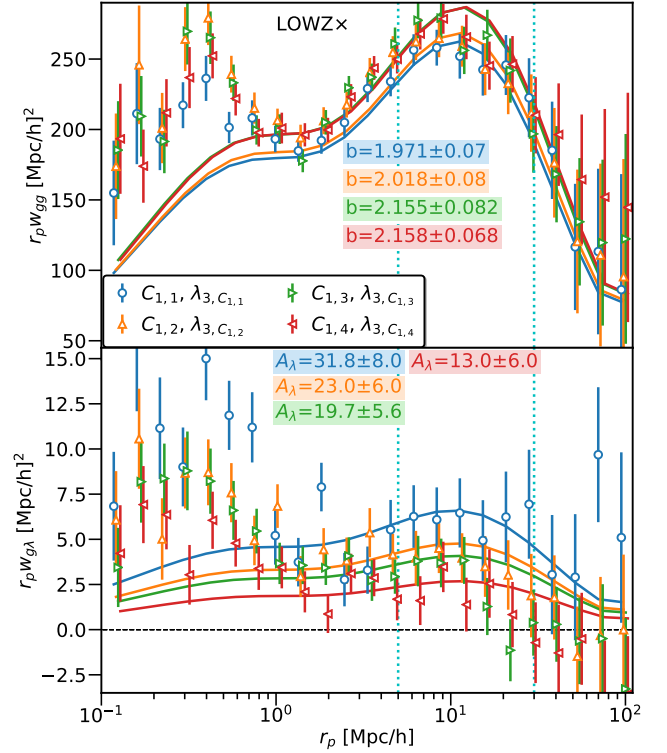


Figure C4. Splitting the Lowz C_1 sample into four subsamples based on color, similar to the original color split. Similar to the original color split, we find a strong evolution with color even within the C_1 sample, with redder samples showing larger FP amplitude, A_λ .

on large scales, we then perform the measurements with the re-weighted randoms. Re-weighting using Ipoly pixelization biases the measurement on small scales, likely because the pixelization from is too fine and randoms start following the true underlying distribution of galaxies (if randoms perfectly followed galaxies, correlation function will be zero). Pixelization using jackknife regions on the other hand is good enough to correct for the systematics while keeping the measurement unbiased. Measurement using this pixelization thus leads to unbiased and more optimal measurement, with errors on the galaxy bias estimates lower by $\sim 30\%$.

Thus for subsamples, we will re-weight the randoms using the weights from jackknife pixelization. Also, to avoid biases we will use the cross correlations between the subsample and the parent sample wherever possible as the δ_{sys} for full sample is very small. Using re-weighted randoms is advantageous for cross correlations as well to obtain the optimal measurements.

E2 Null test

In FP cross correlation measurements for the LOWZ sample, the signal is lower than the best fit model on large scales, which is likely due to some large scale photometric systematics. To test source and potential impact of such a contamination, we show the two null tests for the cross correlation measurements in figure E2.

In the first test, we randomly shuffle the measurement of λ_3 between galaxies to break any possible correlations

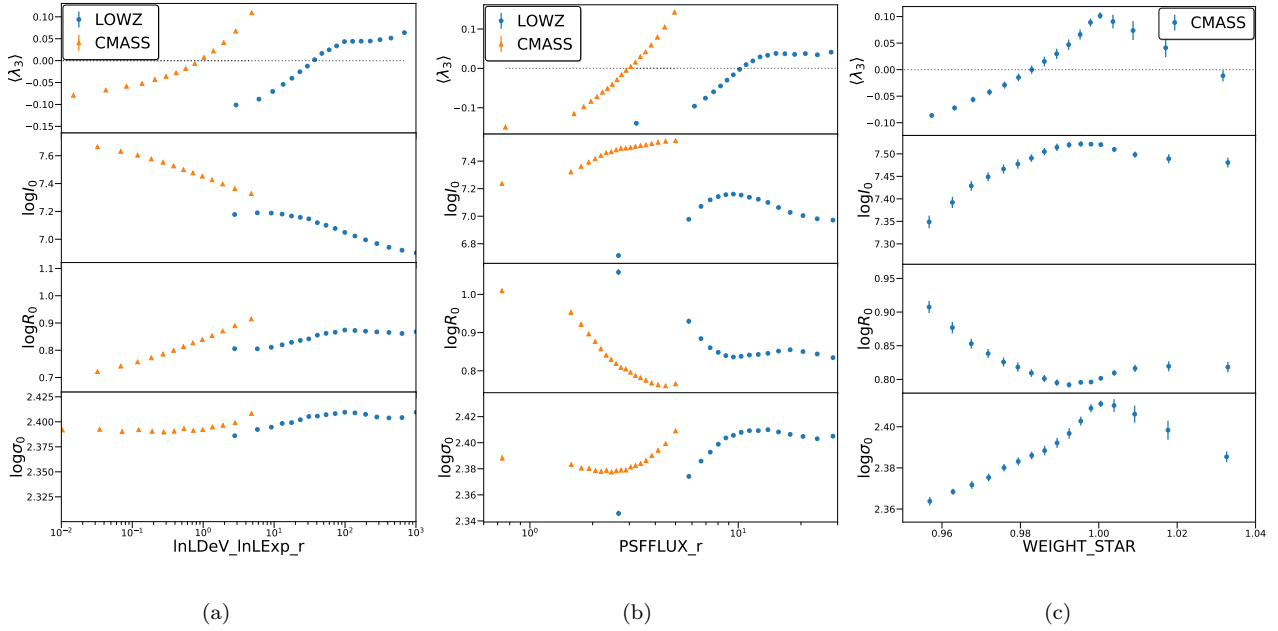


Figure D1. Mean FP residuals (top panel) and galaxy properties (lower 3 panels) as function of various systematics, a) the difference in log likelihood of de Vaucouleurs (DeV) and exponential (Exp) profile fits to the galaxies, b) PSF flux in r band, c) the star weights assigned to CMASS galaxies (LOWZ galaxies are not assigned these weights). There is considerable dependence of the FP residuals on these systematics, though this is primarily driven by the dependence of the estimated luminosity and size on these systematics.

between λ and the galaxies. However, this shuffling is done in narrow redshift bins, so that any possible contributions from the redshift variations in $\langle \lambda_3 \rangle$ will still be present in the cross correlation measurement (see eq. (21)). For the randomly shuffled λ_3 , we detect null correlation and fitting our model for the FP cross correlations, the $A_\lambda = 0.2 \pm 1.3$ value obtained is consistent with zero as expected, ruling out any significant contributions from redshift dependent variations in $\langle \lambda_3 \rangle$ to our main results.

In the second test, we measure the cross correlations at large line of sight separations, $100 < |\Pi| < 500 h^{-1} \text{Mpc}$. For such large line of sight separations, we expect the cross correlation signal to be small (including contributions from weak gravitational lensing). As shown in figure E2, we detect a negative signal on large scales, though the measurement is also very correlated across the bins. When fitting our fiducial model (which assumes measurement is at small Π), we obtain $A_\lambda = 2 \pm 3.3$ to be consistent with zero. This is due to the fact that the systematics causing the non-zero measurement also contribute to the covariance and hence down weighting those scales in the model fits. Contributions from systematics to the covariance are also the reason that the error on A_λ for large Π test is significantly larger than compared to the shuffled test.

These tests suggest that the impact of systematics is likely to be negligible on the A_λ constraints we obtained in section 4.

E3 v Estimator

To remove the impact of any additive systematic with slowly varying correlation function, we define

$$v(r_p, r_0) = \frac{2}{r_p^2} \int_{r_0}^{r_p} dr'_p r'_p w_{g\lambda}(r'_p) - w_{g\lambda}(r_p) + \frac{r_0^2}{r_p^2} w_{g\lambda}(r_0)$$

(E5)

This parameter is independent of the additive systematics with a scale independent correlation function and is in general less sensitive to the systematics with weak scale dependence, as we observe in the measurements of $w_{g\lambda}$. Note that the v parameter is analogous to the Υ parameter defined in the context for galaxy-galaxy lensing by Baldauf et al. (2010). Under the assumption of angular symmetry, v with $r_0 = 0$ is analogous to w_{g+} measured for the intrinsic alignments. In this section we will present results with $r_0 = 0.2 h^{-1} \text{Mpc}$.

In figure E3 we show the comparison of $w_{g\lambda}$ and v parameters. We fit the same model as w_{g+} to the v with the correct constant factor as expected for the FP instead of intrinsic alignments. v measurements are relatively more consistent with the expected scaling from the model as it is expected to be less susceptible to the effects of the systematics. In figure E4, we show the comparison of the amplitude A_λ obtained after fitting $w_{g\lambda}$ versus the A_λ obtained after fitting v . v parameter leads to higher A_λ . This is likely because v is less susceptible to the impact of additive systematics, which have negative sign leading to lower $w_{g\lambda}$ (negative $w_{g\lambda}$ on larger scales).

In figure E5, we show a comparison of the v obtained from FP cross correlations and also from the intrinsic alignment of the galaxies. The two measurements are expected to have same scaling, with FP correlations having lower amplitude by factor of 3 (the constants in the model for IA and FP differ by factor of 3). On small scales, IA is expected to be lower as the satellite galaxies show lower alignments because the orbital motion can lower the alignments but does not significantly affect the size correlations (assuming angular symmetry of mass distribution). On large scales, we observe FP and IA to have similar amplitude, which is con-

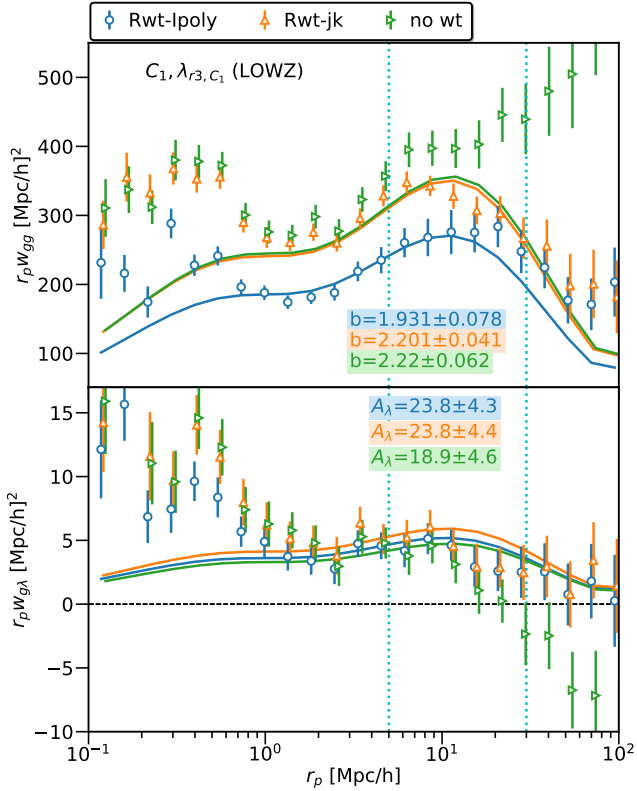


Figure E1. Auto correlations of the LOWZ- C_1 sample and the impact of the re weighting the randoms. Splitting the LOWZ sample by color affects the selection function (in the plane of sky). This results in bias in the measurements at large scales, as shown by the green (no wt) points. We attempt to correct this by re weighting the randoms by the fraction of galaxies that are in C_1 sample compared to the full sample ($Rwt = N_{gal,C_1}/N_{gal,LOWZ}$). For blue points (Rwt-IPoly), we compute weights in the each IPoly region while for orange point (Rwt-jk), we compute weights in each jackknife region ($\sim 80 \text{ deg}^2$). For the case of (Rwt-IPoly), clustering is biased low which is because IPoly regions are too small and the re-weighted randoms are also clustered similar to galaxies. Re weighting on size of jackknife regions on the other hand makes clustering nearly unbiased. Note that even though signal is biased, the galaxy-bias (b_g) is fairly similar across all three cases. This is likely because the systematics from selection function also affect the covariance, down weighting the bins that are biased and also increasing the error on b_g .

sistent with the observation that A_λ is larger than A_I by a factor of ~ 3 (note that our model fits are most sensitive to scales $5 \lesssim r_p \lesssim 10 h^{-1} \text{Mpc}$). Finally we note that the comparison is not strictly fair as the effects of higher order terms from density weighting can still be different in v derived from FP and IA.

APPENDIX F: RSD ANALYSIS

F1 Posterior distribution for the model parameters

In this work, we use three different methods to obtain parameter posteriors: 1) Maximum a posteriori (MAP) estimation and Laplace approximation, using the hessian of the log posterior to obtain the inverse covariance matrix,

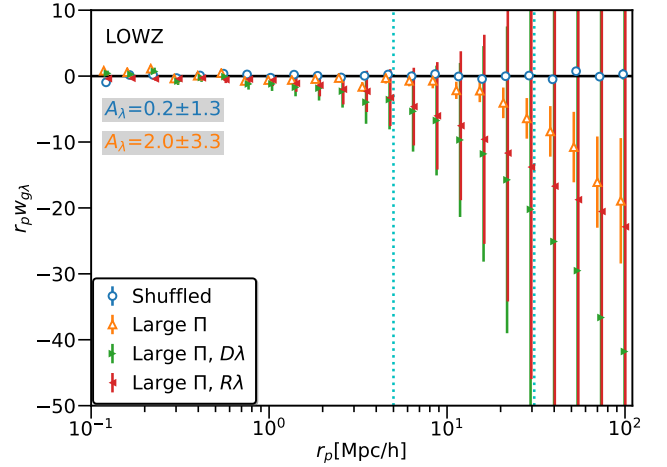


Figure E2. Null tests for the cross correlation measurement $w_{g\lambda}$. Blue points (Shuffled) show the results from shuffling the λ between different galaxies, which gives results consistent with zero as expected. Note that the shuffling is done in the narrow redshift bins, so that we do not null the impact of variations in the $\langle \lambda \rangle$ as function of redshift. Our results suggest that such effects are much smaller than the size of the noise in our measurements. Orange points (large Π) show the measurements in the large line of sight bins, where we expect null signal in the absence of significant contributions from lensing. There is significant non-zero signal at large scales, though the bins are very correlated and the overall significance of the signal is small. We fit our model to the measurement (fixing galaxy bias $b_g = 1.85$) and A_λ is consistent with zero at $\lesssim 1\sigma$. We also show the measurements of $D\lambda/RR$ and $R\lambda/RR$ separately (solid red and green points) that contribute to the estimator of $w_{g\lambda} = D\lambda/RR - R\lambda/RR$.

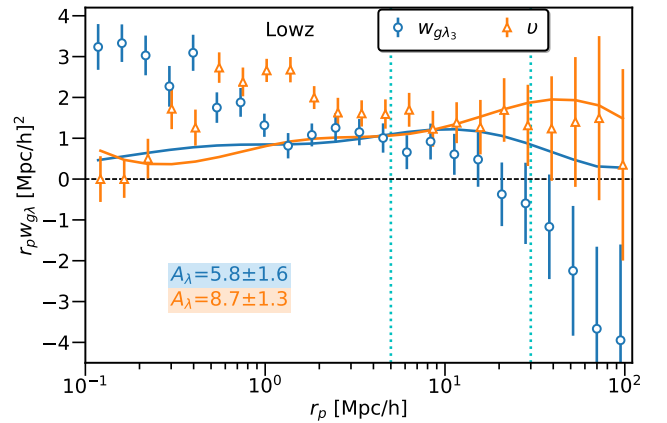


Figure E3. Comparison of FP cross correlation measurement and model fits, using $w_{g\lambda}$ and v estimators. Converting $w_{g\lambda}$ to v reduces the impact of systematics with weakly varying correlation function and leads slightly higher A_λ .

2) MCMC sampling of the likelihood, assuming Gaussian covariance between multipoles, and 3) optimization-based posterior inference method called EL₂O from Seljak & Yu (2019). We obtain the full posterior distributions for each of our 11 model parameters using three aforementioned methods. We find that the posteriors obtained from EL₂O agree well with the MCMC posteriors, while MAP can get the peak of the posterior incorrect. This is more evident in the

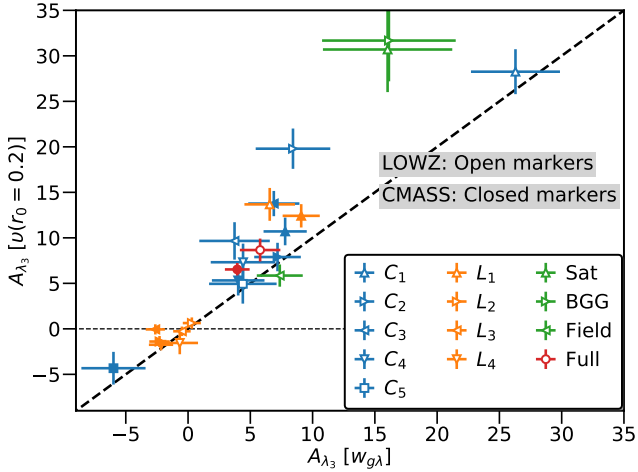


Figure E4. Comparison of A_λ values obtained using $w_{g\lambda}$ compared to the values obtained using v . Using the v parameter removes some effects of the additive systematics and hence leads to relatively higher values of A_λ . However, these values do not change any of the conclusion in the main part of the paper derived using $w_{g\lambda}$ as the qualitative trends do not change.

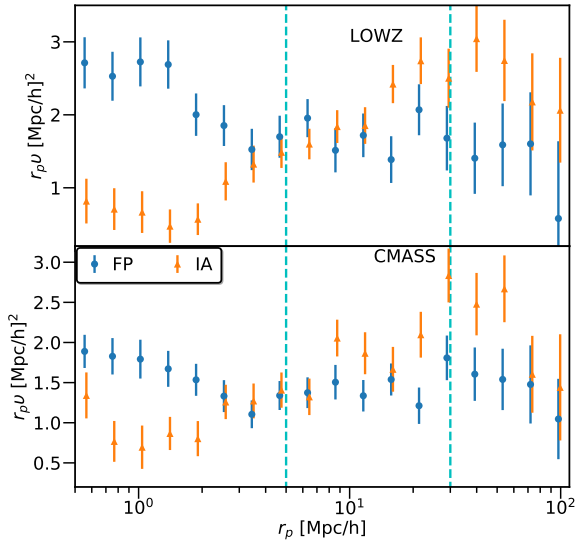


Figure E5. Comparison of v parameter from the fundamental plane to that obtained with the intrinsic alignments of the galaxies (we convert w_{g+} to also v). Under the assumptions of the model, i.e. intrinsic alignments sourcing the FP residuals, the two measurements are expected to have the same scaling but different amplitude by factor of 6. On small scales, we expect some deviations as the satellites show very small IA on small scales.

case of the posteriors for parameters which are most non-Gaussian. More detailed analysis about the comparison can be found in Seljak & Yu (2019). In this work we use the EL2O method to obtain the model parameter posteriors.

F2 Null test

Following appendix E2, in narrow redshift bins we randomly shuffle the measurements of FP residuals between galaxies. We perform 100 random splits of each galaxy sample (LOWZ and CMASS for NGC and SGC regions), creating a pair of subsamples per each split. Finally, we measure the difference in the parameters $f\sigma_8$ and $b_1\sigma_8$ for each pair. As shown in figure F1, for all galaxy samples the difference in both parameters is consistent with the null detection, as expected: $\Delta f\sigma_8$: -0.009 ± 0.031 and -0.007 ± 0.041 for LOWZ NGC and SGC respectively and 0.006 ± 0.024 and -0.008 ± 0.031 for CMASS NGC and SGC respectively. In figure 13, we find that $\Delta f\sigma_8$ measurements are statistically consistent with the null result, and consequently they are equivalent to being drawn from the distributions in figure F1.

In addition to the random splits of the galaxy sample, we take 100 MultiDark-Patchy mock catalogues to estimate the size of the error bars of RSD constraints. We separate each PATCHY mock into two subsamples based on their stellar masses. We call the subsample with its stellar mass greater than the sample mean the “brighter half”, and the remaining subsample with smaller stellar mass is called the “dimmer half”. This mimics the FP cut in section 4.3.1 because stellar masses are strongly correlated with the galaxy luminosity and consequently FP residuals as observed in section 4.1.2. We note that there is considerable scatter between FP residuals and galaxy luminosity and hence the FP cuts are a ‘noisy’ version of the cuts based on stellar mass. Combined with random cuts presented earlier, these cuts provide the two limit for the cuts based on FP residuals. In the left panel of figure F2, we show the best-fit $f\sigma_8$ and $b_1\sigma_8$ parameters we obtain by fitting the RSD model to the measured multipoles from subsamples of 100 LOWZ NGC mocks. In agreement with appendix C, the subsample with a higher luminosity, the brighter half, has a higher galaxy bias. $f\sigma_8$ measurements, on the other hand, are consistent across two subsamples. In the right panel of figure F2, we measure $\Delta f\sigma_8$ and $\Delta b_1\sigma_8$ between subsamples by subtracting the values of the dimmer half from that of the brighter half. For LOWZ NGC, we obtain $\Delta f\sigma_8 = -0.054 \pm 0.049$. Similarly, we measure the propagated errors of $\Delta f\sigma_8$ for all galaxy samples: $\sigma(\Delta f\sigma_8) = 0.049, 0.060, 0.030$, and 0.047 , for LOWZ NGC, LOWZ SGC, CMASS NGC, and CMASS SGC, respectively. We also create 4 luminosity subsamples, $L_1 - L_4$ with L_1 being brightest and L_4 being faintest, from the PATCHY mocks, according to their stellar masses. We follow the convention that $L_1 - L_3$ contain 20% of galaxies each, while L_4 contains 40%. As shown in figure F3, we find the decreasing trend of galaxy bias with luminosity, confirming our observation in appendix C. Moreover, figure F3 shows that $f\sigma_8$ measurements are consistent across all luminosity subsamples.

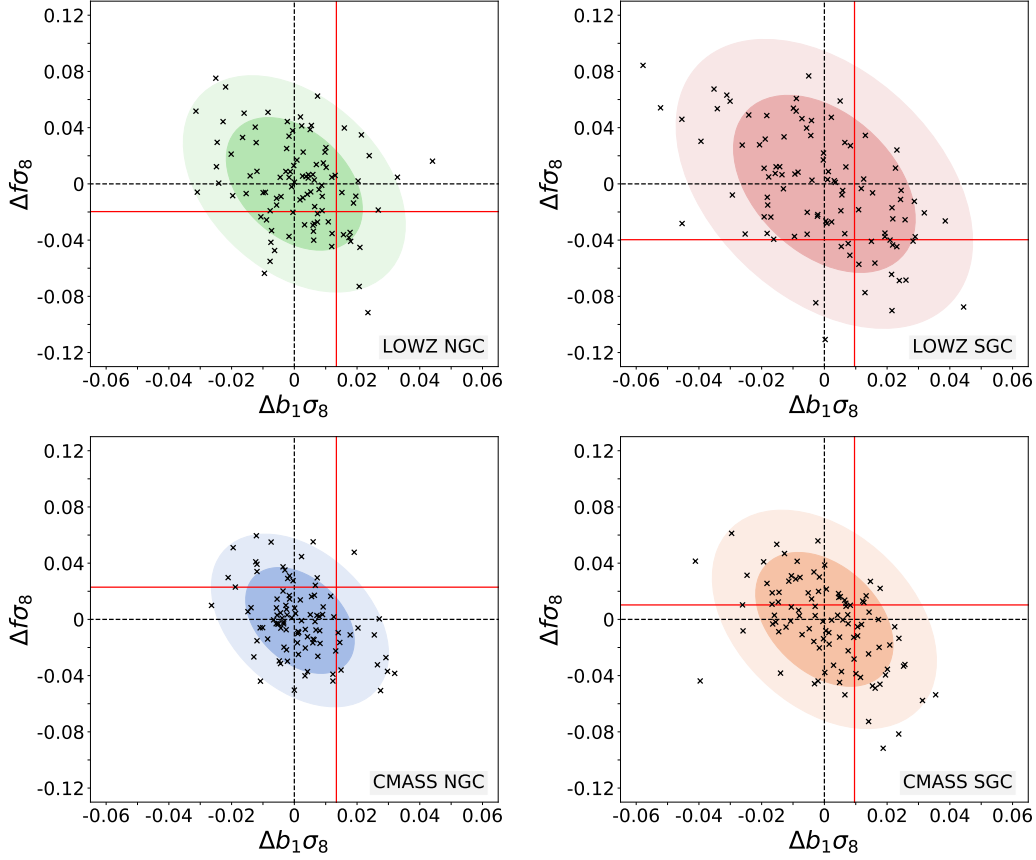


Figure F1. Null test for $\Delta f\sigma_8$ and $\Delta b_1\sigma_8$ measurements. We take 100 random splits for each galaxy sample and measure the difference in $f\sigma_8$ and $b_1\sigma_8$ for each pair of random split subsamples. Black dotted points present the measurements for each pair, showing that both measurements are consistent with the null detection, as expected. Colored confidence ellipses correspond to 68% and 95% probability contours. Red solid lines indicate the measurement from the λ_1 split in figure 13. All $\Delta f\sigma_8$ measurements in figure 13 are consistent with being drawn from the null distributions.

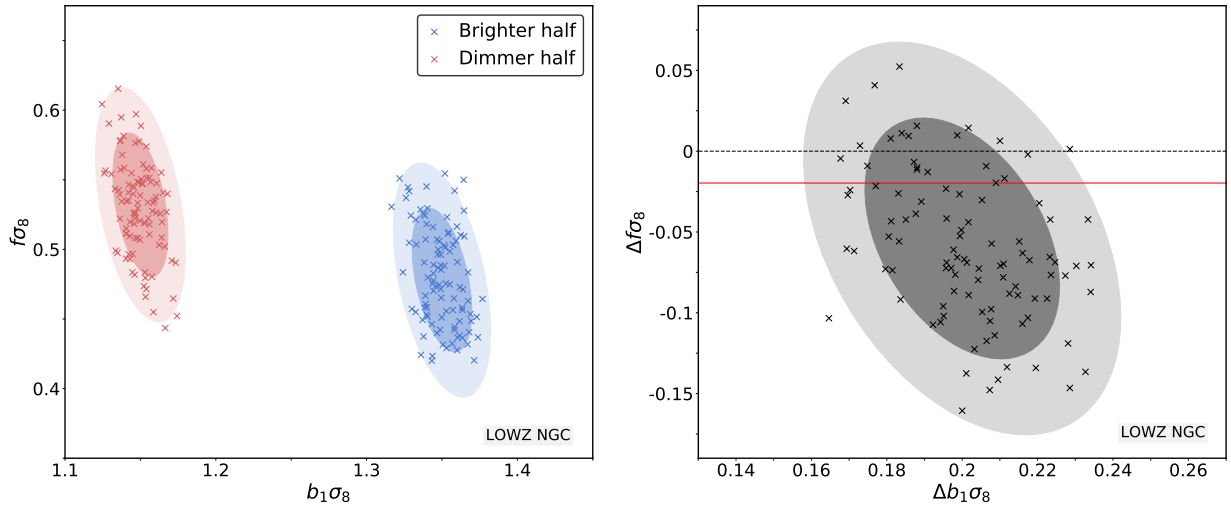


Figure F2. Measuring errors on $\Delta f\sigma_8$ and $\Delta b_1\sigma_8$. *Left:* We mimic the FP cut on the MultiDark-Patchy mock catalogues by separating each mock into two subsamples according to their stellar masses: “brighter half,” (blue) the subsample with its stellar mass greater than the sample mean, and “dimmer half,” (red) the remaining subsample with smaller stellar mass. We note the FP cut is a ‘noisy’ version of this cut as λ is correlated with luminosity with considerable scatter. We show the measurements of $f\sigma_8$ and $b_1\sigma_8$ parameters from both subsamples. In agreement with appendix C, we find that a more luminous galaxy has a higher bias. $f\sigma_8$ measurements, on the other hand, are consistent across two subsamples. *Right:* $\Delta f\sigma_8$ and $\Delta b_1\sigma_8$ measurements, with the values of the dimmer half subtracted from the brighter half. Similar to figure F1, red solid line indicates the measurement from the λ_1 split in figure 13.

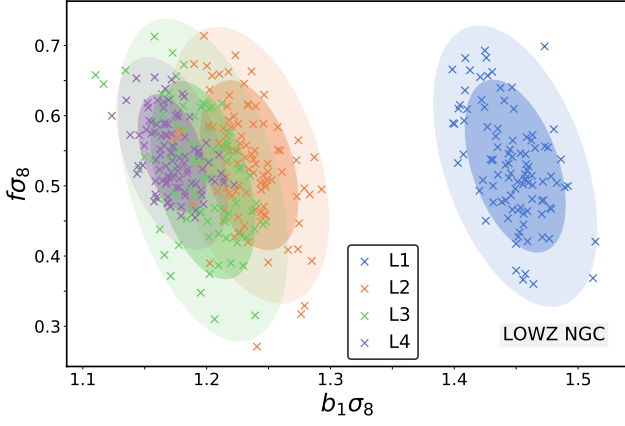


Figure F3. Similar to figure F2. Measurements of $f\sigma_8$ and $b_1\sigma_8$ from 4 luminosity subsamples, $L_1 - L_4$ with L_1 being brightest and L_4 being faintest, of the MultiDark-Patchy mock catalogues. We find the decreasing trend of galaxy bias with luminosity, while $f\sigma_8$ measurements are consistent across all subsamples.